nature communications

Article | Article in Press

https://doi.org/10.1038/s41467-026-78905-y

Contrasting epigenetic dynamics in chromosome arms and pericentromeres during ROS1-induced plant immune memory

Received: 18 August 2025

Accepted: 6 October 2026

Published online: 31 October 2026

Check for updates

Adam Hannan Parker[1] ✉, Peijun Zhang[1], Kwok Yin Man[1], Louis Tirot[1], Stephen A. Rolfe[1], Lisa M. Smith[1], Samuel W. Wilkinson[1,2] & Jurriaan Ton[1] ✉

Immune memory enables plants to respond more effectively to recurrent pathogen infections. Epigenetic changes in DNA methylation and small RNAs have been implicated, yet how their temporal dynamics govern immune memory establishment and erasure remains unclear. Using a chemically inducible system to activate the DNA demethylase REPRESSOR OF SILENCING 1 (ROS1) in Arabidopsis, we establish immune memory against biotrophic pathogens that persists for up to two weeks. Memory establishment coincides with reduced small RNA accumulation and DNA methylation along chromosome arms, including at promoters of genes involved in salicylic acid–dependent immunity and DNA damage repair. These changes are progressively reversed during immune memory erasure. In contrast, transposon-rich pericentromeres retain elevated small RNA and DNA methylation levels, consistent with a CLASSY3-associated redistribution of RNA-directed DNA methylation. Our findings show that transient ROS1 activity drives contrasting epigenetic responses across chromosomal regions, shaping both the establishment and erasure of plant immune memory.

After recovering from stress by pests or pathogens, plants can acquire an enhanced defensive capacity to better resist similar challenges later in life. This induced resistance is based on a form of immune memory, which spans the period between recovery and secondary challenge[1,2]. Depending on the plant species and the intensity of the stress experienced, this immune memory can persist in newly formed tissues for extended periods after the initial exposure to stress[3–8]. A growing body of evidence indicates an important role for epigenetic mechanisms in regulating plant immune memory[6,9]. In particular, cytosine DNA methylation has emerged as a key regulator due to its dynamic response to environmental stress and its capacity for stable transmission across both mitotic and meiotic cell divisions[6,9–13]. Because this memory can incur a fitness cost, epigenetically controlled immune memory is also transient, often reversing in the absence of stress[7,14,15]. The mechanisms underpinning the erasure of immune memory remain unknown.

In plants, cytosine DNA methylation is established by RNA-dependent DNA methylation (RdDM) pathways, which depend on non-coding small RNAs (sRNAs) of 21-24 nucleotides (nt) in length originating from RNA POLYMERASE-II (Pol-II) or Pol-IV transcripts[16,17]. Pol-IV is targeted to specific tissues and genomic loci by the chromatin remodelling factors CLASSY 1-4 (CLSY1-4)[18,19]. These sRNAs associate with ARGONAUTE proteins and guide them to nascent transcripts produced by Pol-V that share sequence similarity, leading to the recruitment of DOMAINS REARRANGED METHYLTRANSFERASE 1 and/or 2 (DRM1/2) and the de novo methylation of adjacent cytosines[16,20]. Once established, DNA methylation is maintained via different pathways depending on the cytosine context (CG, CHG, or CHH; H = A, T, or C). METHYLTRANSFERASE 1 (MET1) and CHROMOMETHYLASE 3

[1]Plants, Photosynthesis and Soil Cluster, School of Biosciences, The University of Sheffield, Sheffield, UK. [2]Department of Biology, Centre for Novel Agricultural Products, The University of York, York, UK. ✉e-mail: a.hannanparker@sheffield.ac.uk; j.ton@sheffield.ac.uk

(CMT3) maintain DNA methylation in CG and CHG contexts, respectively, while CMT2 and RdDM machinery maintain DNA methylation at CHH sites[16,21]. DNA methylation is crucial for the silencing of transposable elements (TEs) – mobile genetic elements that cause large-scale modifications in the genome when activated[9]. In non-stressed vegetative tissues of *Arabidopsis thaliana* (Arabidopsis), RdDM activity is largely confined to gene-transposon boundaries in chromosome arms, whereas CMT-dependent DNA methylation primarily targets TE-rich heterochromatic regions near the centromeres (pericentromeres)[18,21,22].

The removal of DNA methylation is mediated by bifunctional 5-methylcytosine DNA glycosylase/lyases that act through the base excision repair pathway[23]. In Arabidopsis, there are four of these DNA demethylases: REPRESSOR OF SILENCING 1 (ROS1), DEMETER (DME), DEMETER-LIKE 2 (DML2), and DML3[23]. Of these, ROS1 is the most abundant in leaves, where it actively antagonises RdDM at gene-transposon boundaries[23–26]. Numerous studies have demonstrated that mutation of *ROS1* (*ros1* mutants) causes elevated DNA methylation at TEs in the proximity of protein coding genes, resulting in reduced activation of environmentally responsive genes following exposure to biotic and abiotic stress stimuli[5,23,25]. Furthermore, *ros1* mutants cannot establish long-term immune memory against *Spodoptera littoralis* caterpillars upon seedling treatment with jasmonic acid (JA)[7], and fail to develop heritable immune memory against the oomycete pathogen *Hyaloperonospora arabidopsidis* (*Hpa*) after parental infection with the bacterium *Pseudomonas syringae* pv. *tomato* DC3000 (*Pst*)[5]. Hence, ROS1-dependent removal of DNA methylation is emerging as a key feature of adaptive immune responses to biotic stress. However, *ros1* mutant lines exhibit constitutive DNA hypermethylation at loci that are typically lowly or moderately methylated in wild-type plants, which means the role of highly methylated ROS1 targets during biotic stress remains unexplored[6,9]. Moreover, the constitutive nature of *ros1* mutation limits the ability to study the dynamic and reversible epigenetic changes associated with ROS1-induced immune memory.

In this study, we have used a chemically inducible gene construct to transiently activate ROS1 in Arabidopsis, thereby establishing epigenetic immune memory against pathogens. We show that the establishment of this memory is associated with loss of DNA methylation and RdDM-associated sRNAs in chromosome arms alongside transcriptional activation of key defence genes. By contrast, transient ROS1 induction has opposing effects on sRNA accumulation and DNA methylation in transposon-rich pericentromeric regions, involving CLSY3-dependent redistribution of RdDM. Together, these findings reveal the dynamic epigenomic responses underlying ROS1-driven immune memory and identify candidate gene targets and mechanisms that may be leveraged for crop protection strategies.

Results

The *XVE:ROS1-YFP* system allows for transient and dose-dependent activation of ROS1

To induce ROS1 activity in a dose-dependent manner, we transformed Arabidopsis with a 17β-estradiol (E2)-inducible ROS1-YFP construct, which is based on the XVE transactivating system (Fig. 1a)[27,28]. Treatment of *XVE:ROS1-YFP* plants with E2 induces a conformational change in the XVE receptor, enabling it to bind to LexA operator sequences which activates *ROS1-YFP* expression (Fig. 1a, b). We transformed wild-type Col-0 to avoid the pleiotropic effects on epigenetic homoeostasis and plant immunity of constitutive ROS1 loss in *ros1* mutants[24,25].

To validate the inducibility of the *XVE:ROS1-YFP* system, we quantified E2-induced ROS1-YFP accumulation by epifluorescence microscopy in hydroponically grown seedlings. Relative YFP fluorescence was measured 24 h after E2 treatment across a range of E2 concentrations in two independent *XVE:ROS1-YFP* lines – line 5 (L5) and line 7 (L7) – and in Col-0 (negative control; Fig. 1c). A two-way ANOVA revealed a significant genotype × treatment interaction for relative YFP fluorescence ($F = 6.2$; df = 10,90; $p < 0.001$). Both L5 and L7 exhibited fluorescence levels significantly above background (Col-0) at E2 concentrations ≥1 μM (Tukey post-hoc, $p_{adj} < 0.05$).

To assess the persistence of E2-induced ROS1-YFP accumulation, we quantified YFP fluorescence in L5, L7, and Col-0 plants relative to DMSO-treated control plants at 6-, 24-, and 48-h post treatment (hpt) with 5 or 25 μM E2 (Fig. 1d). We performed a repeated-measures ANOVA with genotype and E2 dose as between-subject factors, and hpt as a within-subject factor. The three-way interaction between genotype, E2 dose, and hpt was not significant ($F = 0.1$; df = 4, 36; $p > 0.05$), but there was a significant genotype × hpt interaction ($F = 6.4$; df = 4, 36; $p < 0.001$), indicating that ROS1-YFP dynamics varied by genotype over time, independent of E2 dose. YFP fluorescence in L5 and L7 significantly increased at 24 hpt ($q < 0.05$) before returning to Col-0 levels by 48 hpt ($q > 0.05$). Only L5 showed significantly higher YFP fluorescence than Col-0 at 6 hpt ($q < 0.05$; Fig. 1d). These results indicate that while early induction kinetics differ slightly between the two *XVE:ROS1-YFP* lines, E2 consistently induces transient ROS1-YFP accumulation, peaking at 24 hpt, with expression ceasing or the protein degrading by 48 hpt, regardless of dose.

To confirm the inducibility of the *XVE:ROS1-YFP* construct under conditions used for plant-pathogen assays, we sprayed soil-grown plants with 25 μM E2 at 14 days after sowing (DAS). At 24 hpt, *ROS1* transcript levels were quantified by RT-qPCR, revealing a ~200-fold increase in *XVE:ROS1-YFP* L5 and L7 (two-sided t-test, $p < 0.05$; Fig. 1e). In contrast, Col-0 plants showed no change in *ROS1* expression or YFP signal upon this E2 treatment (two-sided t-test, $p < 0.05$; Fig. 1e, f). DMSO-treated L5 and L7 showed a minor but statistically significant increase in *ROS1* transcripts (1.7x and 2.3x, respectively) relative to Col-0 (two-sided t-test, $p < 0.05$; Fig. 1e), but this did not correspond with increased YFP signal in leaves (Fig. 1f). By comparison, E2-treated L5 and L7 displayed strong YFP signals at 24 hpt that co-localised with nuclear DAPI staining, confirming nuclear localisation of ROS1-YFP (Fig. 1f). Together, these results indicate that despite mild leakiness, the *XVE:ROS1-YFP* system is highly E2-dependent, enabling robust and transient accumulation of ROS1-YFP in Arabidopsis under different growth conditions.

Ectopic ROS1 induction results in transient immune memory against (hemi-)biotrophic pathogens

The *ros1-4* mutant of Arabidopsis is more susceptible to the biotrophic oomycete *Hpa* and the hemi-biotrophic bacterium *Pst*[5,25]. To examine whether ROS1 overexpression induces resistance to these pathogens, we treated Col-0, L5, and L7 seedlings twice with E2 or DMSO before spray-inoculating 2-days-post-treatment (2 dpt) with either *Hpa* (Waco9) or bioluminescent *Pst luxCDABE*[29,30] (*Pst-Lux*; Fig. 2a). Colonisation by *Hpa* was analysed microscopically at 5 days post inoculation (dpi) by assigning trypan blue-stained leaves to *Hpa* colonisation classes, ranging from I (no colonisation) to IV (severe colonisation and sporulation)[31], whereas bacterial colonisation by *Pst-Lux* was quantified non-destructively over multiple days, using bioluminescence intensity as a quantitative measure of colonisation[29,30] (Fig. 2c, d).

Treatment of Col-0 with either DMSO or E2 resulted in similar levels of colonisation by *Hpa* (Fisher's exact-test, $q > 0.05$), indicating that E2 itself has no direct effect on *Hpa* (Fig. 2b). In contrast, E2 treatment of both *XVE:ROS1-YFP* lines resulted in strongly reduced *Hpa* colonisation compared to DMSO-treated plants (Fisher's exact tests: L5: $q < 0.001$; L7: $q < 0.001$), while DMSO-treated *XVE:ROS1-YFP* lines were as susceptible as DMSO- and E2-treated Col-0 plants (Fisher's exact tests, $q > 0.05$; Fig. 2b). Hence, ectopic induction of ROS1 by two successive E2 treatments induces resistance against *Hpa*.

A linear mixed-effects model, which accounted for dpi and the random effect of pot was fitted to our *Pst-Lux* bioluminescence data from two to four dpi. Likelihood ratio tests between the full model and reduced models revealed statistically significant effects of genotype

https://doi.org/10.1038/s41467-026-78905-y

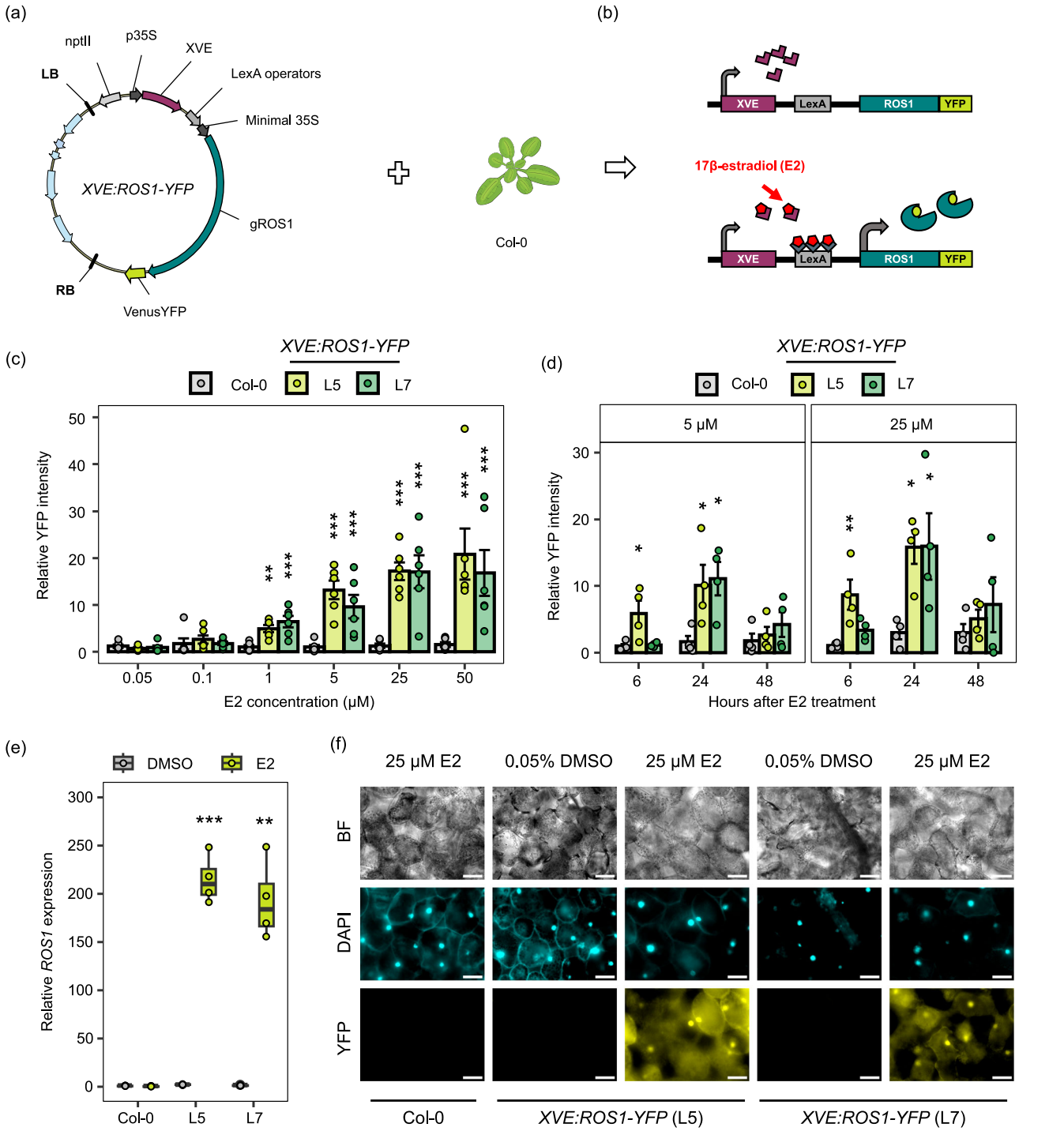


Fig. 1 | Characterisation of *XVE:ROS1-YFP* lines. a Plasmid map of estradiol (E2)-inducible *XVE:ROS1-YFP* construct used to transform Col-0. **b** Schematic of the XVE E2-inducible system. **c** ROS1-YFP protein accumulation at 24 h after treatment of 7-day-old hydroponically grown seedlings (Col-0, *XVE:ROS1-YFP* line 5; L5, and *XVE:ROS1-YFP* line 7; L7) with increasing E2 concentrations. Data points represent relative YFP fluorescence intensities, normalised by plant area, from biologically replicated seedlings ($n = 6$). Shown are data relative to the mean YFP fluorescence intensity value from DMSO-treated Col-0 seedlings. Asterisks indicate a statistically significant difference in relative YFP fluorescence intensity compared to E2-treated Col-0 (Tukey post-hoc tests; * $p_{adj} < 0.05$, ** $p_{adj} < 0.01$, *** $p_{adj} < 0.001$). **d** ROS1-YFP protein accumulation at 6-, 24-, and 48-h after treatment (hpt) with 5- or 25-μM E2 in 7-day-old hydroponically grown seedlings. Data points represent YFP intensity values from biological replicates ($n = 4$) relative to the mean YFP intensity value from DMSO-treated controls within a given genotype and timepoint. For each time-point, pairwise two-sided t-tests against Col-0 were performed; *p*-values were adjusted by false discovery rate (FDR; * $q < 0.05$, ** $q < 0.01$, *** $q < 0.001$). In (**c**, **d**), bars represent mean values with error bars representing ± standard error of the mean. Exact p_{adj}-values are provided in the Source data file. **e** Quantification of *ROS1* transcripts by RT-qPCR at 24 hpt after spraying soil-grown Col-0, L5, and L7 plants with 25 μM E2 or 0.05% DMSO at 14 days after sowing (DAS). Data points represent relative expression values of individual biological replicates ($n = 4$) normalised to the mean relative expression value of DMSO-treated Col-0 plants. Box plots show median (centre line), with 25th and 75th percentiles (box bounds), and whiskers extending to most extreme value within 1.5x IQR. Asterisks indicate a statistically significant difference between treatments within a genotype (two-sided t-test; ** $p = 0.003$, *** $p = 0.0004$). **f** ROS1-YFP protein accumulation was imaged at 24 h by epi-fluorescence microscopy after the same treatment as (**e**). DAPI and YFP images were pseudo-coloured cyan and yellow, respectively. Scale bars, 50 μm.

https://doi.org/10.1038/s41467-026-78905-y

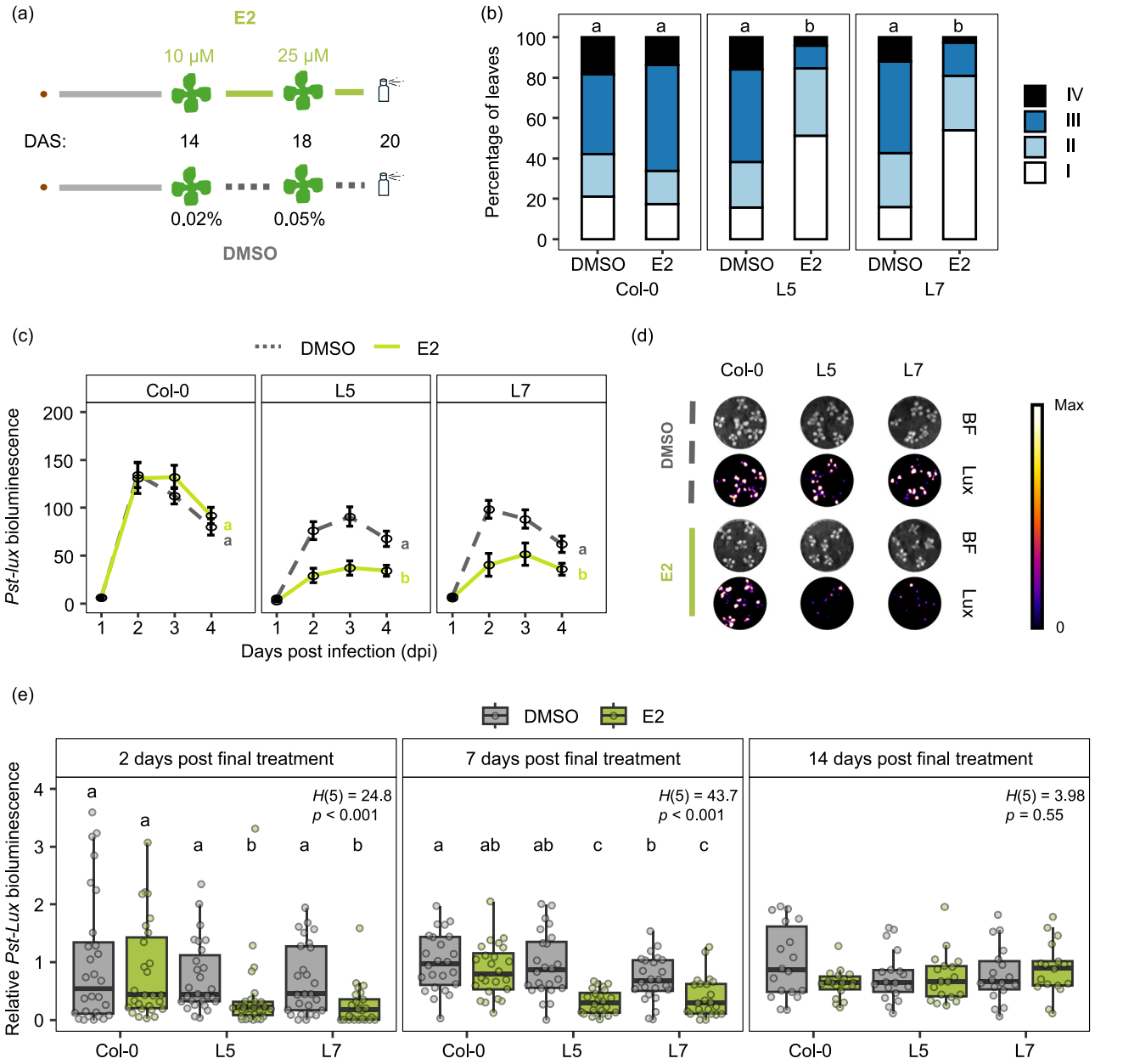


Fig. 2 | Quantification of ROS1-induced immune memory against (hemi-)biotrophic pathogens. a Experimental setup to quantify induced resistance by E2-induced ROS1 against the (hemi)biotrophic pathogens *Hpa* and *Pst-Lux*. Col-0, L5, and L7 plants were treated twice with E2 or DMSO at 14 days after sowing (DAS) (10 µM E2 or 0.02% DMSO) and 18 DAS (25 µM E2 or 0.05% DMSO). 2 days post the final treatment (20 DAS; 2 dpt), plants were inoculated with *Hpa or Pst-Lux*. **b** At 5 dpi with *Hpa*, individual leaves (72–80 leaves from 4 pots containing 3–5 individual plants) were stained by trypan-blue and microscopically assigned *Hpa* colonisation classes[31]. Different letters indicate significant differences in colonisation class distributions (Fisher's exact test; $q < 0.05$). **c** Colonisation by *Pst-Lux* was quantified 1–4 dpi by bioluminescence intensity in 8 pots per genotype per treatment containing 1–7 plants. Points with error bars represent mean *Pst-Lux* bioluminescence values across all plants ($n = 31$–41) ± SEM. Different letters indicate statistically significant differences in the progression of *Pst-Lux* colonisation between 2 and 4 dpi (linear mixed effects model; two-sided estimated marginal means post-hoc; Tukey-adjusted $p_{adj} < 0.05$). **d** Representative examples of *Pst-Lux* bioluminescence at 2 dpi. **e** Duration of ROS1-induced immune memory against *Pst-Lux*. Col-0, L5, and L7 plants were treated with DMSO or E2, as shown in (**a**), and inoculated with *Pst-Lux* at 2 ($n = 25$–31), 7 ($n = 23, 24$), or 14 ($n = 17, 18$) days post final treatment (2 dpt, 7 dpt, 14 dpt). *Pst-Lux* colonisation was quantified by bioluminescence 2- or 3-dpi and expressed relative to the Pst-Lux bioluminescence of DMSO-treated Col-0 within each timepoint. Box plots show median (centre line), with 25th and 75th percentiles (box bounds), and whiskers extending to most extreme value within 1.5x IQR. If a significant treatment effect on relative *Pst-Lux* colonisation was detected (Kruskal-Wallis, $p < 0.05$), Conover-Iman post-hoc tests with a Benjamini-Hochberg correction were performed. Different letters indicate significant differences ($p_{adj} < 0.05$). Exact *p*-values and sample sizes are provided in the Source data file.

(Col-0, L5, L7; $X^2 = 46.6$, df = 4, $p < 0.001$), treatment (DMSO, E2; $X^2 = 31.7$, df = 3, $p < 0.001$), and the interaction between genotype and treatment ($X^2 = 15.9$, df = 2, $p < 0.001$). Pairwise post-hoc comparisons on the estimated marginal means confirmed that E2-treated *XVE:ROS1-YFP* lines sustained significantly lower levels of *Pst-Lux* colonisation compared to the corresponding DMSO controls ($p_{adj} < 0.05$; Fig. 2c). In contrast, DMSO- and E2-treated Col-0 plants sustained similar *Pst-Lux* colonisation dynamics ($p > 0.05$; Fig. 2c, d). Characterisation of three additional independent *XVE:ROS1-YFP* lines (L6, L30 and L32) which showed varying levels of E2-induced YFP fluorescence confirmed that reduced ROS1 induction results in lower resistance to *Pst-Lux*

(Supplementary Fig. 1a, b). Thus, ectopic induction of ROS1 induces resistance against *Pst-Lux*.

Our initial bioassays used two successive E2 treatments with increasing concentrations, reasoning that sustained ROS1 activation would better mimic the progressive epigenetic changes triggered by escalating stress from a virulent pathogen. Single treatments – either 10 μM E2 at 14 DAS or 25 μM E2 at 18 DAS – did not consistently induce resistance against *Pst-Lux* at either 7- or 2-dpt (Supplementary Fig. 1d–g). In contrast, both a repeated high-dose induction regime (four applications of 25 μM E2 between 14-20 DAS) and an incremental dual-dose regime (10 μM at 14 DAS followed by 25 μM at 18 DAS) reproducibly enhanced resistance in both lines at 2 dpt (Supplementary Fig. 1d–g). Therefore, we adopted the dual-treatment protocol for all subsequent experiments to ensure a reliable resistance phenotype for downstream analyses.

To assess the durability of ROS1-induced immune memory, we challenged Col-0, L5, and L7 plants with *Pst-Lux* at 2 dpt, 7 dpt, or 14 dpt after the final treatment (Fig. 2e). Resistance against *Pst-Lux* was evident in *XVE:ROS1-YFP* lines at both 2 dpt and 7 dpt, but not at 14 dpt (Fig. 2e). Furthermore, progeny of E2-treated *XVE:ROS1-YFP* lines did not show enhanced resistance to either *Pst-Lux* or *Hpa* relative to progeny from DMSO-treated control plants (Supplementary Fig. 2). These results indicate that, while transient ROS1 induction is sufficient to induce resistance against biotrophic pathogens, this immune memory is lost within 7–14 days. Thus, the *XVE:ROS1-YFP* system offers a tractable model to study the establishment, maintenance, and often-overlooked erasure of plant immune memory.

The establishment of ROS1-induced immune memory is associated with major changes in the transcriptome and DNA methylome

To investigate the molecular drivers of ROS1-induced immune memory, Col-0, L5, and L7 plants were treated twice with E2 or DMSO (Fig. 2a) and biologically replicated ($n = 3$) aerial tissues were harvested 48 h after the final treatment. DNA and RNA were extracted from the same pool of tissues before sequencing for DNA methylation (whole-genome bisulfite sequencing; WGBS), ribosome-depleted total RNA, and small RNAs (sRNAs). Principal component analysis (PCA) of all three datasets revealed that ROS1-induction was the primary source of variance (Supplementary Fig. 3b–d). Crucially, E2- and DMSO-treated Col-0 samples clustered together in all three datasets, demonstrating that the global shifts in DNA methylation, gene expression, and sRNA abundance were driven by ectopic ROS1 induction rather than by E2 treatment itself.

E2-treated *XVE:ROS1-YFP* lines, but not Col-0, exhibited reduced DNA methylation across chromosome arms in all cytosine contexts (allC, CG, CHG, CHH) relative to DMSO-treated controls (Fig. 3a; Supplementary Fig. 4). In contrast, pericentromeric regions were less affected, with some loci displaying CHG hypermethylation in E2-treated L5 and L7 (Fig. 3a; Supplementary Fig. 4). DNA hypomethylation by ROS1 was less pronounced within gene bodies than in their flanking regions (Supplementary Fig. 4a, b), whereas hypomethylation was stronger within TE bodies compared to their flanking regions (Supplementary Fig. 4b). Analysis of differentially methylated regions (DMRs) identified thousands of hypomethylated DMRs in E2-treated L5 (11,067) and L7 (12,158) plants, but only 25 in E2-treated Col-0 plants. Few hypermethylated DMRs were detected across all genotypes: 22 in L5, 18 in L7, and 30 in Col-0 (Supplementary Fig. 4c; Supplementary Data 1). After merging DMRs across all cytosine contexts, 4,971 overlapping hypomethylated DMRs were identified in E2-treated L5 and L7 plants (Supplementary Fig. 5a). These consistent hypo-DMRs were highly enriched at gene-TE boundary regions, with the strongest enrichment occurring at TEs in the promoter regions of protein-coding genes (Supplementary Fig. 5b). Analysis of two recently published ChIP-seq datasets for ROS1[26,32] revealed significant enrichment of endogenous ROS1 binding within our hypo-DMRs relative to randomly selected genomic regions, in both independent datasets (Kruskal–Wallis $p < 0.001$; Conover–Iman $q < 0.05$; Supplementary Fig. 5c, d). Thus, our results support previous characterisations of ROS1 in Arabidopsis[24,25,32] and indicate that the recombinant ROS1-YFP protein is functionally active as a DNA demethylase.

The ROS1-induced transcriptome is enriched with genes controlling salicylic acid-dependent immunity and DNA damage response

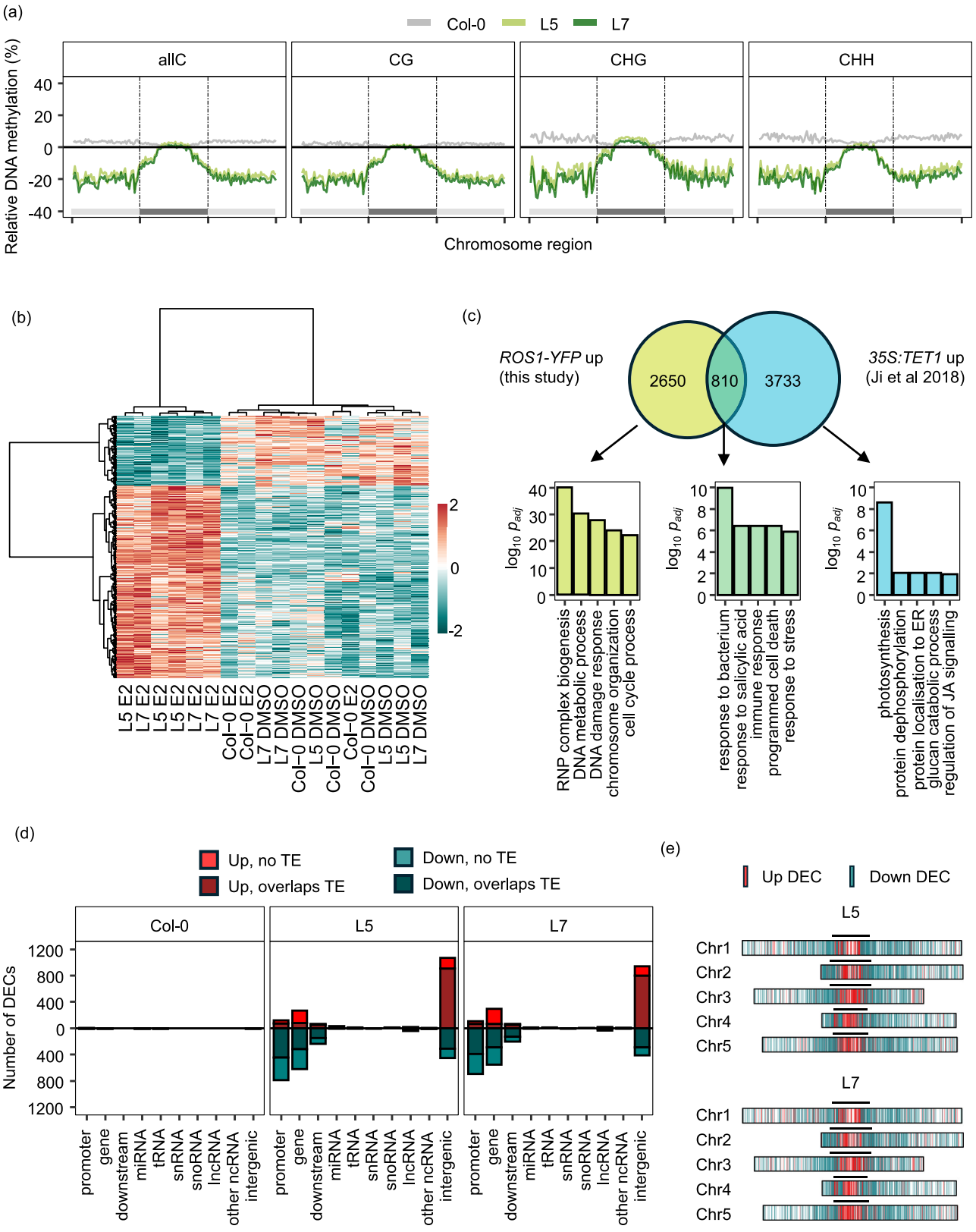
E2-treatment of L5 and L7, but not Col-0, profoundly altered the transcriptional profile, with a strong correlation between both lines ($r = 0.94$, $n = 4724$, $p < 0.001$; Supplementary Fig. 6a; Supplementary Data 2). Hierarchical clustering of all differentially expressed genes (DEGs) separated replicate samples of E2-treated *XVE:ROS1-YFP* lines from all other treatment groups (Fig. 3b). This analysis identified two distinct DEG clusters: genes upregulated in E2-treated *XVE:ROS1-YFP* lines ('up' cluster; $n = 3460$) and genes downregulated in these lines ('down' cluster; $n = 1264$). The majority of DEGs were protein-coding genes (95% and 96% in the up- and downregulated clusters, respectively), with the remainder consisting of TE-derived transcripts and non-coding RNAs (Supplementary Fig. 6c; Supplementary Data 2). Gene ontology (GO) enrichment analysis showed that upregulated DEGs were significantly associated with biological processes related to chromatin organisation, DNA damage response, and immunity, whereas downregulated DEGs were primarily enriched for GO terms linked to photosynthesis (Supplementary Fig. 6b; Supplementary Data 3).

Activation of the DNA damage repair pathway by ectopically induced ROS1 likely results from the enzyme's DNA glycosylase/lyase activity[23]. To separate the transcriptional effects of ROS1-induced DNA hypomethylation from those caused by DNA damage, we compared the upregulated DEGs ('up' cluster; Fig. 3b) with upregulated DEGs by TEN-ELEVEN TRANSLOCATION 1 (TET1), based on a previous characterisation of *35S:TET1* overexpression lines[33] (Supplementary Data 2). Since TET1 converts 5mC to oxidised derivatives that are poor substrates for DNA methyltransferases[33,34], enhanced TET1 activity results in passive loss of DNA methylation without directly inducing DNA damage in plants. Genes uniquely upregulated in E2-treated *XVE:ROS1-YFP* lines were enriched for GO terms linked to DNA damage and chromatin organisation (Fig. 3c), whereas the 810 genes commonly upregulated in both E2-treated and *35S:TET1* lines were significantly enriched with genes related to SA-dependent immunity (Fig. 3c; Supplementary Data 3). Accordingly, we conclude that the epigenetic DNA demethylation activity of ROS1, rather than its DNA glycosylase/lyase activity, enhances SA-dependent immunity in Arabidopsis.

Enhanced ROS1 activity induces contrasting patterns of small RNA accumulation between chromosome arms and pericentromeres

To characterise the ROS1-induced changes in sRNA profiles, we mapped sRNA clusters against the Arabidopsis genome using ShortStack[35,36]. E2-treated L5 and L7, but not Col-0, showed thousands of differentially expressed sRNA clusters (DECs) compared to the DMSO-treated controls (Fig. 3d; Supplementary Fig. 7a). Downregulated DECs primarily occurred at gene-TE boundaries, while upregulated DECs were more abundant at intergenic TEs (Fig. 3d). Most of these DECs were composed of 24-nucleotide (nt) sRNAs, which accounted for 97% of downregulated and 82-85% of upregulated DECs in both lines (Supplementary Data 4; Supplementary Fig. 7b). Only 17 DECs were identified in E2-treated Col-0, demonstrating a negligible chemical effect of E2 on sRNA expression patterns (Supplementary Figs. 3g, 7b; Supplementary Data 4). Plotting the genomic locations of all up- and downregulated DECs across the five nuclear chromosomes revealed a dramatic disparity in their distribution: downregulated

https://doi.org/10.1038/s41467-026-78905-y



DECs were predominantly located along chromosome arms, whereas upregulated DECs mostly mapped to the pericentromeric regions (Fig. 3e). This pattern correlates with the spatial distribution of DNA methylation changes in E2-treated *XVE:ROS1-YFP* lines (Fig. 3a; Supplementary Fig. 7d), highlighting opposing epigenetic dynamics in chromosome arms and pericentromeric regions following transient increases in ROS1 activity.

A subset of ROS1-inducible genes with reduced promoter DNA methylation and/or sRNA abundance includes regulators of immunity and DNA damage responses

DNA methylation can function as a *cis*-regulatory mechanism that suppresses gene expression in Arabidopsis[5,25]. For example, promoter hypermethylation of the defence gene *RLP43* in *ros1* mutants inhibits transcription factor binding and *RLP43* transcription[25,37,38]. To identify

Fig. 3 | Genome-wide characterisation of the methylome, transcriptome, and sRNAome following transient ROS1 induction. a Chromosome-level metaplots of DNA methylation in E2-treated plants. Shown are the mean percentage differences in cytosine methylation relative to DMSO-treated plants in Col-0 (grey), L5 (light green), and L7 (dark green). For each chromosome, average DNA methylation was calculated for 50 equally sized bins in the left arm, the pericentromeric region, and the right arm before averaging across replicates ($n = 3$) and chromosomes. **b** Heatmap projection of all 4,724 differentially expressed loci/genes (DEGs) between E2- and DMSO-treated plants within a genotype. Heatmap-projected values represent per gene Z-scores of transformed normalised read counts from 3 biological replicates for each genotype-treatment combination. Scores were clustered by both DEG (Euclidean, Ward) and sample (Pearson correlation, Ward). **c** Venn diagram showing the overlap of upregulated DEGs ($p_{adj} < 0.05$) in E2-treated *XVE:ROS1-YFP* L5 and L7 (derived from figure **b**) and upregulated DEGs in *35S:TET1* lines ($p_{adj} < 0.05$)[33]. Shown are the top 5 GO enrichment terms in order of statistical significance for biological process for the overlapping DEG set (green) and the unique DEG sets (yellow and blue *for XVE:ROS1-YFP* and *35S:TET1*, respectively). RNP = ribonucleoprotein; JA jasmonic acid. **d** Annotation counts of differentially expressed sRNA clusters (DECs) from E2-treated L5 and L7, as compared to DMSO-treated L5 and L7, respectively. DECs were annotated using Araport11[64], and TAIR10 TE annotations. Counts of up- and downregulated DECs are shown above and below the $y = 0$ line, respectively. **e** Distribution of DECs across the five Arabidopsis chromosomes for L5 and L7. Red and blue vertical rectangles superimposed on the chromosomes represent up- and downregulated DECs, respectively. Black lines above the chromosomes mark pericentromeric regions.

more candidate genes with similar hallmarks of *cis*-regulation by DNA methylation, we performed a genome-wide screen for protein-coding genes that were transcriptionally induced in E2-treated *XVE:ROS1-YFP* lines ($p_{adj} < 0.05$) and whose promoters showed simultaneous hypomethylation (hypo-DMR, $p_{adj} < 0.05$) and/or reduced 24-nt sRNA abundance (24-nt down-DEC, $p_{adj} < 0.05$; Supplementary Fig. 8d). The latter criterion was included because reduced 24-nt sRNA abundance was associated with hypomethylated DMRs in our dataset (Supplementary Fig. 9a). The screen identified 253 and 271 candidate genes in L5 and L7, respectively, of which 173 were shared between both lines (Supplementary Fig. 8e; Supplementary Data 5). The set of shared gene candidates were significantly upregulated in the globally hypomethylated *mddcc* mutant (Supplementary Fig. 9b)[39] and included the previously characterised ROS1-regulated defence gene *RLP43*[25], supporting the validity of our approach. Other candidates included the immune regulators *NON-EXPRESSOR OF PATHOGENESIS-RELATED GENES 1* (*NPR1*)[40] and *THIOREDOXIN HOMOLOG 5 (TRXH5)*[41,42], as well as DNA damage response regulators *ATAXIA TELANGIECTASIA AND RAD3-RELATED* (*ATR*) and *E2FC*[43], which aligns with the GO enrichment analysis of the total transcriptome (Supplementary Fig. 6b; Supplementary Data 3). Nevertheless, promoter hypomethylation was not globally associated with increased gene expression (Supplementary Fig. 9c), suggesting that most ROS1-responsive DEGs are regulated indirectly, consistent with previous reports[5,25,44,45].

Long-read direct DNA sequencing reveals increased non-CG methylation at the (peri)centromeres after ROS1 induction

Our WGBS analysis indicated that pericentromeric regions are less affected by ROS1-induced DNA hypomethylation (Fig. 3). Since the reduced DNA methylation by ROS1 anticorrelated with the abundance of sRNAs (Fig. 3a, e), we hypothesised that the limited hypomethylation in pericentromeric regions is not caused by reduced ROS1 targeting but rather by increased RdDM activity in these regions that counteracts ROS1 activity. However, the highly repetitive nature of pericentromeres limits epigenetic characterisation of these regions, since short-read sequencing approaches map poorly to these regions[46–48].

To obtain a more reliable analysis of pericentromeric and centromeric (hereafter referred to as (peri)centromeric) DNA methylation, we leveraged long-read sequencing technology and the centromere-complete Col-CEN reference genome assembly[47]. We restricted this analysis to L5, as our previous phenotypic and molecular analyses demonstrated that L5 and L7 show nearly identical responses to E2, while E2 itself had negligible effects on untransformed Col-0 plants (Figs. 1–4, Supplementary Figs. 1–9). L5 plants were treated twice with either DMSO or E2 (Fig. 2a), after which biologically replicated samples ($n = 3$ per treatment) were sequenced using Oxford Nanopore Technology (ONT-seq)[7]. Reads were mapped to the Col-CEN genome assembly and cytosine methylation was called using DeepSignal-plant[49]. Like the WGBS results (Supplementary Fig. 3b), PCA of DNA methylation revealed a distinct separation between DMSO- and E2-treated L5 plants (Supplementary Fig. 11). Moreover, chromosome-level metaplots of DNA methylation confirmed hypomethylation in chromosome arms, as was also clear from the WGBS data (Fig. 4a, Fig. 3a). However, the improved resolution by ONT-seq and the Col-CEN genome at (peri)centromeres enabled us to detect a much clearer DNA hypermethylation response in these highly repetitive regions after ROS1 induction (Fig. 4a).

The sequence subcontexts of CHG and CHH methylation sites serve as indicators of the mechanisms driving their establishment and/or maintenance[21]. CHG methylation in the CTG and CAG sub-contexts is typical for CMT3-dependent DNA methylation ('CMT3 efficient'), while CHH methylation in the CAA and CTA sub-contexts is typical of CMT2-dependent DNA methylation ('CMT2 efficient'). All other sub-contexts in CHG (CCG) and CHH (CAC, CAT, CCA, CCC, CCT, CTC, CTT) contexts are CMT3- and CMT2-inefficient, and are more likely to be maintained by RdDM[21]. The increased CHH methylation in centromeric and pericentromeric regions did not show a statistical difference between CMT2-efficient and CMT2-inefficient sub-contexts (two-sided Wilcoxon rank-sum test, $p > 0.05$; Fig. 4a). However, for CHG contexts, the relative increase in DNA methylation was significantly greater for CMT3-inefficient contexts compared to CMT3-efficient contexts in (peri)centromeric regions ($p < 0.001$; Fig. 4a). Hence, the increase in non-CG DNA methylation in the (peri)centromeres is not confined to CMT-dependent sub-contexts, indicating involvement of other pathways, such as RdDM[21].

To confirm the contrasting patterns of DNA methylation between chromosome arms and (peri)centromeres, we used DSS[50,51] to select for differentially methylated cytosines (DMCs) between E2- and DMSO-treated L5 plants ($p < 0.05$, absolute change > 10%; Supplementary Data 6). In support of the results depicted in the metaplots (Fig. 4a), this analysis identified tens of thousands of hypomethylated DMCs across all contexts (CG, CHG, CHH) in the chromosome arms, with few hypermethylated DMCs. In contrast, several thousand hypermethylated DMCs were detected in the (peri)centromeres, particularly in the CHG and CHH contexts (Fig. 4b, c). Collectively, our ONT-seq data suggest that transient ROS1 activity triggers a DNA hypermethylation response in (peri)centromeric regions which may act to prevent widespread chromatin de-condensation in these TE-rich regions. Supported by our complementary finding that transient ROS1 activity increases (peri)centromeric sRNA accumulation (Fig. 3), we propose that this protective response is driven by RdDM, rather than by CMT2/3-dependent methylation.

Loss of CLSY3 attenuates ROS1-induced sRNA accumulation in the pericentromeres

In non-stressed vegetative tissues of Arabidopsis, RdDM activity is largely confined to the chromosome arms[18,22]. The genomic distribution of Pol-IV-associated 24 nt sRNAs is coordinated by competing CLSY proteins, which recruit Pol-IV to distinct genomic regions[18,19,52]. CLSY1 predominates in the vegetative tissues, directing Pol-IV RdDM to the chromosome arms, whereas CLSY3/4 are more active in

https://doi.org/10.1038/s41467-026-78905-y

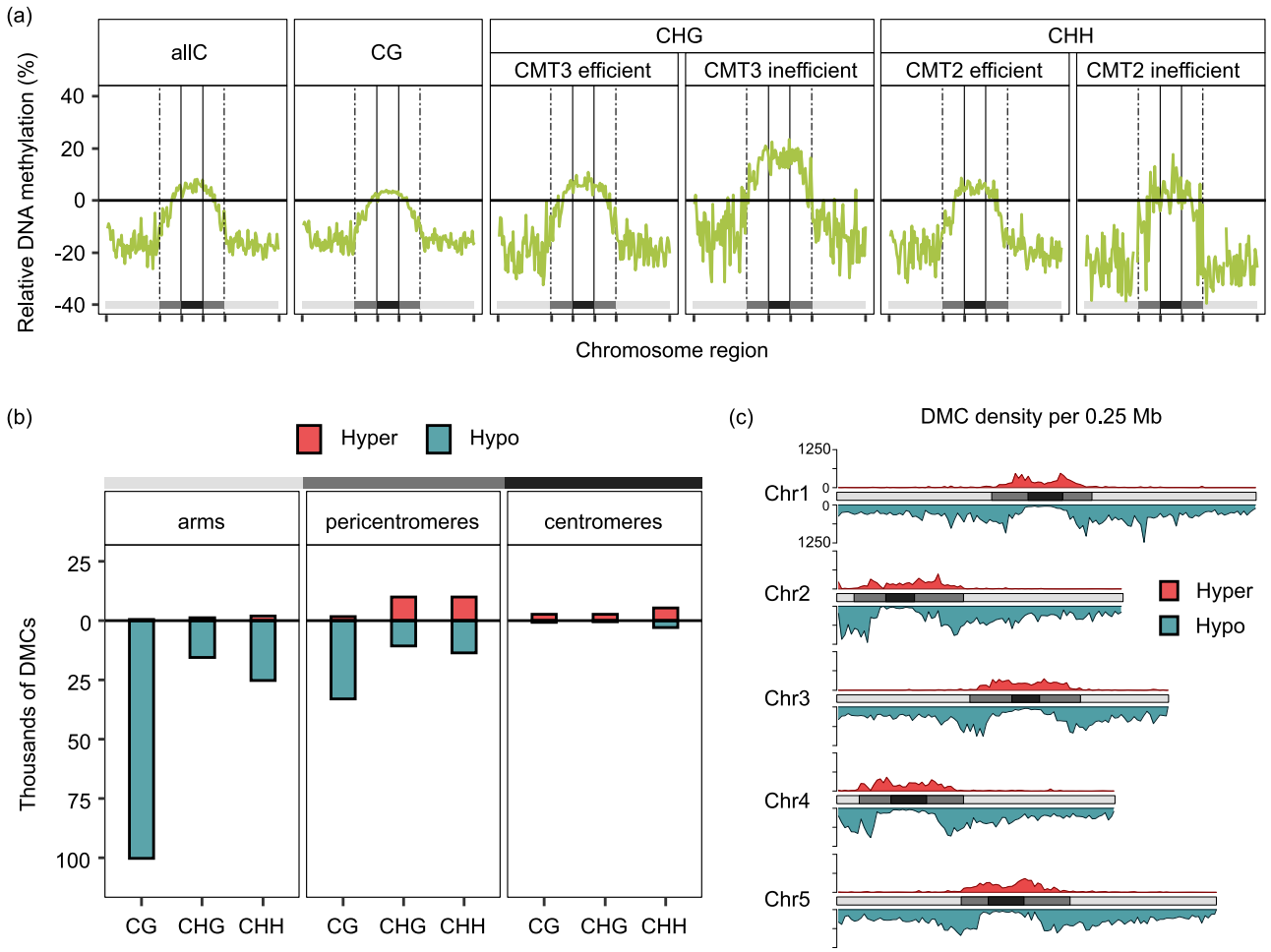


Fig. 4 | Long-read ONT-sequencing analysis of global DNA methylation responses to induced ROS1 activity. a Chromosome-level metaplots showing mean percentage differences in cytosine DNA methylation in E2-treated *XVE:ROS1-YFP* L5 plants relative to DMSO-treated plants, determined by long-read Oxford Nanopore Technology sequencing (ONT-seq) and DeepSignal-Plant[49]. For each chromosome in the Col-CEN genome assembly[48], metaplots were generated by calculating DNA methylation in fixed genomic bins per chromosome: 50 bins for the left arm, 50 bins for the right arm, 20 bins for the centromeric region, and 20 bins for each pericentromeric flank (i.e., 40 bins total for the pericentromeres). DNA methylation was then averaged across biological replicates ($n = 3$), bins, and chromosomes. For CHG and CHH contexts, DNA methylation was calculated separately for CMT2/3-efficient and -inefficient subcontexts[21]. **b** Total counts of differentially methylated cytosines (DMCs; $p < 0.05$, absolute change > 10%)[50,51] in chromosome arms, pericentromeres, and centromeres. Counts of hyper- and hypo-DMCs are shown above and below the $y = 0$ line, respectively. **c** Density of DMCs within 0.25 mega-base (Mb) bins across the 5 chromosomes of the Col-CEN assembly. Light grey, dark grey, and black regions represent chromosome arms, pericentromeres, and centromeres, respectively.

reproductive tissues, directing RdDM towards pericentromeric regions[18,19]. Strikingly, *CLSY3* transcript levels increased approximately sevenfold after E2 induction in *XVE:ROS1-YFP* plants (Fig. 5a; Supplementary Data 2), which we verified by RT-qPCR in an independent experiment (Supplementary Fig. 12a). Since transient ROS1 activation enhanced sRNA accumulation and DNA methylation in (peri)centromeric regions (Fig. 3; Fig. 5), we hypothesised that the elevated *CLSY3* expression contributes to a redistribution of RdDM machinery to these regions. To test this, we introduced the previously characterised *clsy3-1* mutation[19] into our inducible *XVE:ROS1-YFP* line (L5) and compared genome-wide sRNA, DNA methylation, and mRNA profiles between L5 and *clsy3*/L5 plants.

PCA of sRNA profiles revealed clear global differences between *clsy3*/L5 and L5 under both basal (DMSO) and induced (E2) ROS1 conditions (Supplementary Fig. 12c). DECs across all treatment-genotype combinations grouped into four major clusters (Fig. 5b). The two largest clusters (groups 2 and 4; $n = 1487$ and $n = 1475$) displayed a markedly reduced response to E2 in *clsy3*/L5 relative to L5, despite the slightly higher *ROS1* induction in the mutant background (Fig. 5b; Supplementary Fig. 12b). Furthermore, groups 2 and 4 showed clear spatial biases: DECs which were less repressed by ROS1 in *clsy3-1* mutants (group 4) were enriched in the pericentromeres, whereas DECs that were less induced by ROS1 in *clsy3-1* mutants were mostly located in chromosome arms (Fig. 5c). The two smaller clusters, groups 1 ($n = 858$) and 3 ($n = 1{,}002$), representing constitutive increases and decreases in sRNAs by *clsy3-1*, irrespective of treatment, were likewise partitioned between chromosome arms and pericentromeric regions, respectively (Supplementary Fig. 12f–i).

Consistent with these sRNA patterns, PCA of genome-wide DNA methylation revealed global differences between *clsy3*/L5 and L5 plants (Supplementary Fig. 12d). Chromosome-level metaplots indicate that *clsy3*/L5 plants exhibit reduced DNA methylation in the pericentromeric regions and a concomitant increase along chromosome arms, which was more pronounced following E2 treatment (Fig. 5d). The modest magnitude of these DNA methylation changes suggests that additional mechanisms alongside CLSY3 participate in the redistribution of DNA methylation activity. Nonetheless, our combined sRNA and methylome data indicate that *CLSY3* contributes to the redistribution of RdDM from chromosome arms to pericentromeric regions after transient increases in ROS1 activity.

https://doi.org/10.1038/s41467-026-78905-y

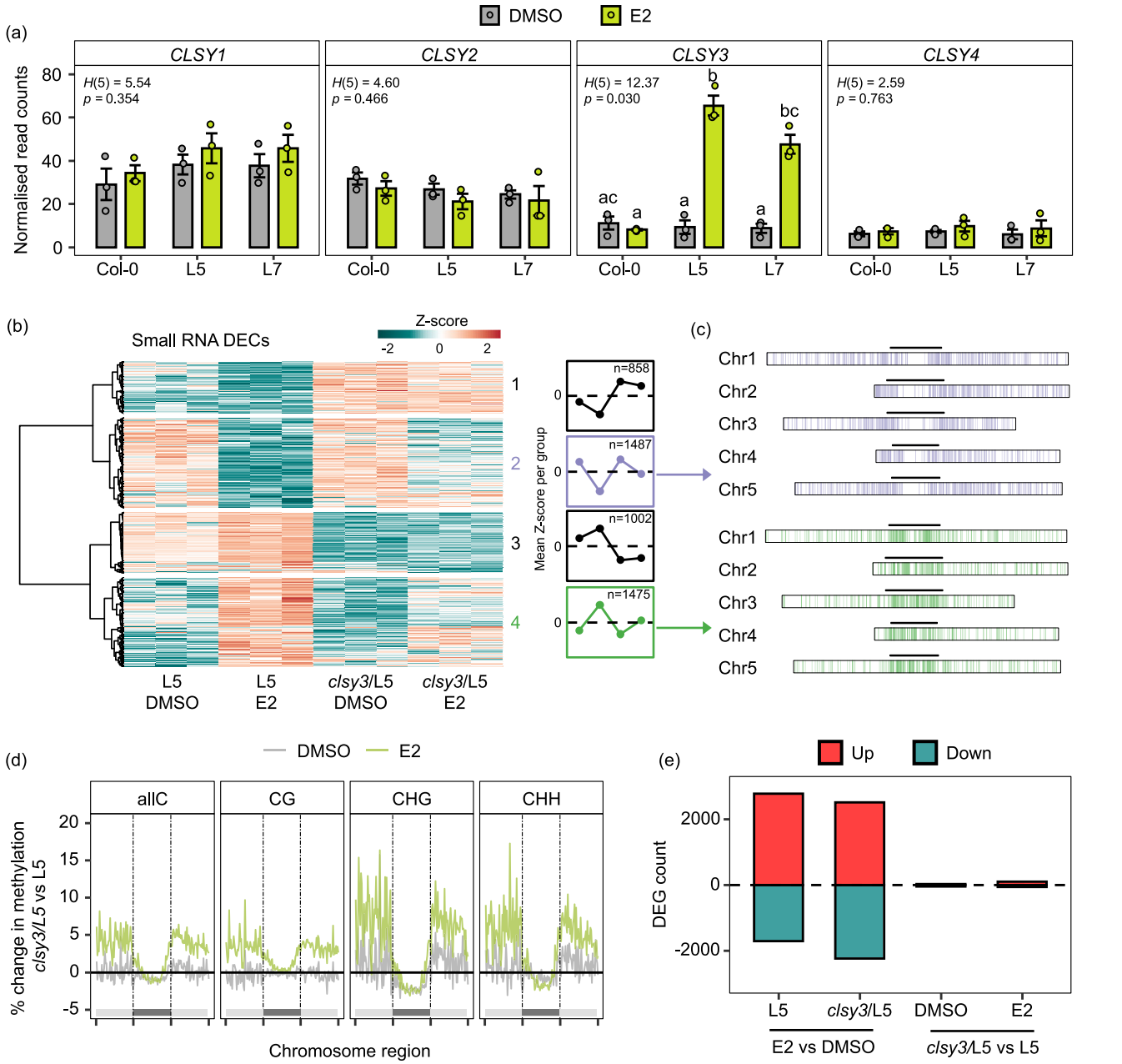
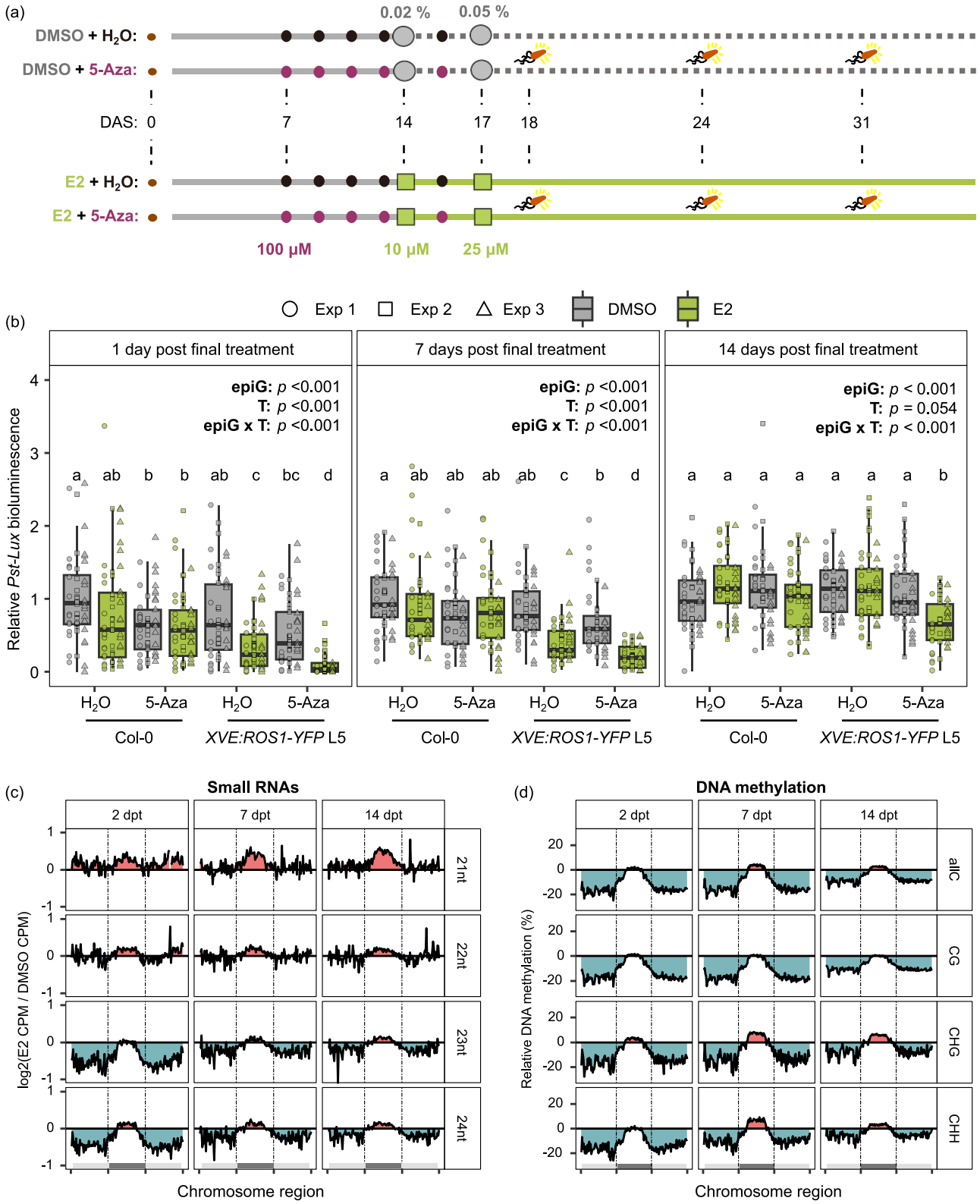


Fig. 5 | Role of CLSY3 in the epigenomic and transcriptomic response to ROS1 induction. a DESeq2-normalised read counts ($n = 3$) of *CLSY* genes in Col-0 and *XVE:ROS1-YFP* lines (L5, L7) 48 h after treatments with two successive DMSO (0.02% and 0.05%) or E2 (10 µM and 25 µM) treatments at 14 and 18 days after sowing (DAS; Fig. 2a). Bars represent mean values with error bars representing standard error of the mean. For each gene, groups which do not share a letter are statistically different (Kruskal-Wallis $p < 0.05$; Conover-Iman post-hoc q-value < 0.05)[75]. Exact p-values are provided in the Source data file. **b** Heatmap showing Z-scores of normalised and transformed sRNA read counts in all identified DECs between genotypes (*clsy3*/L5 vs L5) and treatments (E2 vs DMSO). DECs were identified using ShortStack[35,36] and DESeq2[66]. Each genotype-treatment combination is based on 3 biological replicates. Hierarchical clustering was performed for DECs (Euclidean, Ward), which resolved 4 DEC clusters based on expression patterns. Line graphs show mean Z-scores of DECs within each of these four cluster groups. **c** Genomic location of DECs in group 2 (purple) and group 4 (green) across the five nuclear chromosomes of TAIR10 Arabidopsis genome assembly. Black lines above box mark pericentromeres. **d** Chromosome-level metaplots showing mean percentage difference in DNA methylation in *clsy3*/L5 relative to L5 for DMSO- (grey) and E2-treated (green) plants. Average DNA methylation was calculated for 50 equally sized bins in the left arm, the pericentromeric region, and the right arm before averaging across replicates ($n = 3$) and chromosomes. Dashed lines and dark grey rectangles represent pericentromeres. **e** Shown are total number of all DEGs (DESeq2, $p_{adj} < 0.05$) identified between treatments (E2 vs DMSO) and between genotypes (*clsy3*/L5 vs L5). Up- and down-regulated DEGs are plotted above and below the $y = 0$ line, respectively.

Despite the global impacts of the *clsy3-1* mutation on epigenomic responses to ROS1 activity, PCA of the corresponding polyA-enriched RNA-seq (mRNA-seq) data showed no clear separation between L5 and *clsy3*/L5 under either treatment condition (Supplementary Fig. 12e). Although E2 treatment induced thousands of DEGs in both genotypes (Fig. 6e; Supplementary Data 2), direct comparisons between *clsy3/L5* and L5 identified only a few DEGs under either basal ($n = 80$) or induced ($n = 164$) conditions (Fig. 5e). These results indicate that, despite its role in shaping genome-wide RdDM dynamics, CLSY3 exerts

https://doi.org/10.1038/s41467-026-78905-y



only minor effects on gene expression in leaf tissues, both in the absence and presence of increased ROS1 activity.

DNA re-methylation in the chromosome arms resets ROS1-induced immune memory

Transient increases in ROS1 activity induces resistance against (hemi-) biotrophic pathogens, but this resistance is lost between 7- and 14-days post treatment (Fig. 2e; Supplementary Fig. 2). Since the establishment of this transient immune memory coincided with substantial reductions in DNA methylation and sRNAs along the chromosome arms (Figs. 3–5; Supplementary Figs. 4 and 7), we next investigated whether the reversal of these epigenetic marks drives the erasure of immune memory.

To address this, we introduced the *XVE:ROS1-YFP* L5 transgene into mutant backgrounds impaired in non-CG DNA methylation and/or sRNA production, and assessed the durability of ROS1-induced

Fig. 6 | DNA re-methylation of the chromosome arms drives the loss of ROS1-induced immune memory. a Experimental design to assess the strength and duration of ROS1-induced immune memory against *Pst-Lux* with or without 5-Aza. Col-0 and *XVE:ROS1-YFP* (L5) seedlings received 100 µM 5-Aza or H_2O droplets five times (7, 9, 11, 13, 16 DAS), followed by two sprays of DMSO (0.02% and 0.05%) or E2 (10 µM and 25 µM), at 14 and 17 DAS. Plants were challenged with Pst-Lux at 1, 7, or 14 days after the final E2 treatment (18, 25, 32 DAS). **b** *Pst-Lux* bioluminescence was quantified at 2–3 dpi[44]. For each time point, data from three independent experiments (Exp1-3) were normalised to the mean *Pst-Lux* colonisation values of H_2O-DMSO-treated Col-0 plants before pooling. Two-way ANOVA assessed the statistical significance of the (epi)genotype (epiG; genotype and 5-Aza/H_2O treatment), E2 treatment (T), and their interaction (epiG x T) on relative *Pst-Lux* colonisation. For each timepoint, different letters indicate statistically significant differences between treatment-genotype combinations (Tukey, $p_{adj} < 0.05$). Box plots show median (centre line), with 25th and 75th percentiles (box bounds), and whiskers extending to most extreme value within 1.5x IQR. Exact p_{adj}-values and plant counts are provided in the Source data file (**c**, **d**) Chromosome-level metaplots of (**c**) small RNAs (sRNAs) and (**d**) DNA methylation in L5 at 2, 7 and 14 days post final E2 treatment (2 dpt, 7 dpt, 14 dpt). E2- and DMSO-treatments were performed as shown in Fig. 2a: 10 µM and 25 µM E2, or 0.02% and 0.05% DMSO, at 14 and 18 DAS, respectively. For each chromosome in the TAIR10 genome assembly, (**c**) sRNA counts, or (**d**) mean DNA methylation were calculated in 50 bins for each chromosomal region (left arm, pericentromeres, right arm) and then averaged across replicates ($n = 3$ per timepoint) and chromosomes. Plots show (**c**) mean $\log_2$ fold-changes in sRNA counts per mapped-million (CPM) for 21–24 nt reads, and (**d**) mean percentage differences in DNA methylation for each context (allC, CG, CHG, CHH), relative to DMSO-treated controls. Dashed lines mark pericentromeres; increases and decreases are shaded in red and blue, respectively.

immune memory against *Pst-Lux*. In addition to the *clsy3*/L5 line described above, we generated *cmt3-11*/L5 and *nrpe1-11*/L5 crosses. In non-stressed conditions, the *cmt3-11* mutation primarily affects CHG methylation in pericentromeric regions[53,54], whereas the *nrpe1-11* mutation disrupts RdDM[5,55], leading to non-CG hypomethylation along the chromosome arms[22,54] (Supplementary Fig. 13). None of these mutations prolonged ROS1-induced immune memory against *Pst-Lux* (Supplementary Fig. 14). However, while *cmt3-11* and *clsy3-1* showed no statistically significant effects on *Pst-Lux* colonisation across all timepoints (Tukey $p_{adj} > 0.05$), E2-treated *clsy3*/L5 plants showed a modest increase in *Pst-Lux* colonisation at 7 dpt (Welch's $t = 2.89$, $df = 51.3$, $p = 0.005$) and 14 dpt (Welch's $t = 2.00$, $df = 60.4$, $p = 0.0495$) relative to E2-treated L5 plants. This observation is consistent with the attenuated ROS1-induced DNA demethylation in chromosome arms in the *clsy3-1* background (Fig. 5d), suggesting a minor contribution of CLSY3 to immune memory maintenance. In contrast, the *nrpe1-11* mutation increased basal resistance at later timepoints (Supplementary Fig. 14) consistent with previous reports linking reduced RdDM activity to enhanced immunity[5,56]. This pleiotropic phenotype, however, confounded our assessment of RdDM in the erasure of ROS1-induced immune memory.

To test whether the recovery of DNA methylation at ROS1-demethylated sites (DNA re-methylation) contributes to the erasure of immune memory, we treated L5 seedlings with 5-Azacytidine (5-Aza), a DNA methyltransferase inhibitor that causes genome-wide reductions in DNA methylation[57] (Supplementary Fig. 13). Small droplets of water or 100 µM 5-Aza were applied to the meristems of Col-0 or L5 seedlings starting 7 days before the first DMSO/E2 treatment and ending 1 day before the final DMSO/E2 treatment (Fig. 6a). Aside from mild growth reductions, 5-Aza caused no visible phytotoxicity (Supplementary Fig. 15). Plants were then challenged with *Pst-Lux* at 1 dpt, 7 dpt, and 14 dpt after the second E2 treatment, corresponding to the establishment, maintenance, and erasure of the immune memory, respectively (Fig. 6a). In the absence of ROS1 induction, 5-Aza treatment had a negligible effect on pathogen colonisation, with only a slight increase in resistance in DMSO-treated Col-0 at 1 dpt (Fig. 6b). In contrast, combining E2 and 5-Aza in L5 consistently and synergistically reduced *Pst-Lux* colonisation at all time points relative to E2 treatment alone ($p_{adj} < 0.05$), including at 14 dpt, when ROS1-induced immune memory had otherwise disappeared (Figs. 6, 2e and Supplementary Fig. 14). These results indicate that inhibiting DNA methyltransferase activity with 5-Aza slows the re-methylation of DNA in chromosome arms, which is associated with prolonged ROS1-induced immune memory.

Because the *clsy3-1* and *cmt3-11* mutations, which reduce pericentromeric DNA methylation, did not prolong ROS1-induced immune memory against *Pst-Lux* (Supplementary Fig. 14), we hypothesised that the erasure of immune memory via DNA re-methylation occurs in the chromosome arms. To confirm this, we performed time-resolved epigenomic profiling, tracking sRNA abundance and global DNA methylation from memory establishment (2 dpt) through maintenance (7 dpt) and erasure (14 dpt). Consistent with a role for RdDM in memory erasure, we observed a gradual recovery of sRNAs and non-CG DNA methylation along the chromosome arms that coincided with the loss of ROS1-induced immune memory (Fig. 6c, d). The promoters of our 173 *cis*-regulated gene candidates (Supplementary Fig. 8) remained hypomethylated from 2 dpt to 7 dpt but exhibited significant recovery by 14 dpt (Supplementary Fig. 16). In contrast, ROS1-induced increases in pericentromeric sRNAs and DNA methylation were maintained or even enhanced over the same period, indicating that this response does not control immune memory (Fig. 6c, d). Together, our results indicate that immune memory is epigenetically encoded by transient DNA hypomethylation in the chromosome arms and is reset through progressive re-methylation in these regions.

Discussion

Here, we demonstrate that transient increases in ROS1 activity can establish immune memory against (hemi-)biotrophic pathogens in Arabidopsis. Previous research linked loss of ROS1 function to impaired immunity and transcriptional responsiveness[5,7,25]. However, these studies are confounded by pleiotropic effects associated with constitutive loss of ROS1 function in *ros1* mutants and cannot address the role of loci that are already highly methylated under stress-free conditions. Using an inducible *XVE:ROS1-YFP* system, we have overcome these limitations and provide a framework to dissect the mechanisms underlying the establishment, maintenance, and erasure of epigenetic immune memory in plants. We also identify a set of *cis*-regulated candidate genes displaying increased transcription and reduced promoter DNA methylation after ROS1-YFP induction, which included the immune-regulatory genes *NPR1* and *TRXH5*[40–42] (Supplementary Fig. 10 and Supplementary Data 5). These transcriptional regulators may contribute to the enhanced expression of SA-dependent defence genes (Fig. 3 and Supplementary Fig. 6) and the ROS1-induced immune memory (Fig. 2 and 7; Supplementary Figs. 1 and 14). However, while all hypomethylated DMRs were significantly enriched for ROS1 occupancy in two independent ChIP-seq datasets (Supplementary Fig. 5c, d)[26,32], assessment of ROS1-YFP binding would be required to verify that these individual loci are directly targeted by ROS1 in our inducible XVE system.

Ectopic induction of ROS1 caused significant reductions in DNA methylation along the chromosome arms (Fig. 3) but was accompanied by an unexpected increase in DNA methylation across the (peri) centromeric regions that persisted at least 14 days (Figs. 3a, 5a, 6d). This hypermethylation coincided with increased pericentromeric sRNA accumulation (Figs. 3e, 6c) and an approximate sevenfold increase in *CLSY3* expression (Fig. 5a; Supplementary Fig. 12), suggesting that enhanced ROS1 activity drives CLSY3-associated redistribution of RdDM towards the pericentromeres (Fig. 5)[18,19,52]. Consistent with this model, ROS1 induction in the *clsy3-1* background (*clsy3*/L5) attenuated these patterns: pericentromeric sRNA accumulation was reduced, and depletion of sRNAs from chromosome arms

was less pronounced (Fig. 5). Correspondingly, ROS1-induced DNA hypomethylation in chromosome arms and DNA hypermethylation in pericentromeric regions were both reduced in *clsy3*/L5 (Fig. 5d). These findings support a model in which CLSY3 competes with other CLSY proteins to guide Pol-IV to pericentromeric regions in response to elevated ROS1 activity[19,52]. Thus, while RdDM in unstressed leaf tissues is largely confined to the chromosome arms[18,22], its spatial distribution appears more dynamic under periods of extensive DNA demethylation, such as those triggered by biotic stress[6,9]. Under these conditions, increased pericentromeric RdDM activity may help limit widespread TE activation and preserve genome integrity.

As ROS1-induced immune memory only persisted for seven days before fading (Figs. 2e, 6b; Supplementary Fig. 14), the *XVE:ROS1-YFP* system enabled us to investigate the often-overlooked erasure of immune memory. To address this, we introduced the *XVE:ROS1-YFP* construct into select genetic mutant backgrounds (*clsy3-1*, *cmt3-11*, *nrpe1-11*), and assessed their effects on the establishment, maintenance, and erasure of this memory (Supplementary Fig. 14). While the *cmt3-11* mutation, which primarily affects pericentromeric DNA methylation (Supplementary Fig. 13), had no detectable effect on the strength or duration of the memory, the RdDM-associated mutations, *nrpe1-11* and *clsy3-1*, had notable effects on the resistance phenotype against *Pst-Lux*. Specifically, the *nrpe1-11* mutation, which reduces non-CG methylation along the chromosome arms (Supplementary Fig. 13), resulted in elevated levels of basal resistance to *Pst-Lux* at later timepoints, regardless of ROS1 induction. By contrast, the *clsy3-1* mutation did not enhance nor prolong ROS1-induced immune memory significantly, but it did weakly suppress the resistance from 7 days post treatment (Supplementary Fig. 14). Given that *clsy3*/L5 lines displayed reduced loss of DNA methylation along chromosome arms following ROS1 induction (Fig. 5), these findings collectively suggest that ROS1-induced DNA demethylation followed by re-methylation of chromosome arms drives the establishment and erasure of immune memory, respectively. Complementary experiments with the DNA methyltransferase inhibitor 5-Aza[57] supported this interpretation: 5-Aza not only enhanced ROS1-induced immune memory but also extended its duration by at least 7 days (Fig. 6b), suggesting that DNA re-methylation drives the erasure of immune memory. Indeed, our time-course experiment revealed the ROS1-induced reduction in DNA methylation and 23–24 nt sRNAs along the chromosome arms gradually recovered in parallel with the erasure of ROS1-induced immune memory (Fig. 6c, d; Supplementary Fig. 16), whereas pericentromeric regions showed sustained and, in some cases, enhanced accumulation of sRNAs and DNA methylation at later timepoints (Fig. 6d). Taken together, our findings indicate that transient ROS1-induced immune memory is established through DNA demethylation within chromosome arms and subsequently erased through re-methylation of these regions.

Collectively, our results uncover roles for DNA methylation in both the establishment and erasure of plant immune memory, providing a plausible molecular mechanism underlying the survival and adaptive plasticity of plants in variably stressful environments[14,15]. Beyond advancing our fundamental understanding of ROS1-mediated DNA demethylation, the *XVE:ROS1-YFP* system and the methodologies developed here offer a framework for the controlled introduction of epigenetic variation in plants. More broadly, this opens new opportunities for epigenetic crop breeding and plant protection technologies.

Methods

Plant materials and growth conditions

All experiments were conducted using *Arabidopsis thaliana* (Arabidopsis) lines in the genetic background of Columbia (Col-0). For pot-based experiments, seeds were stratified in 1 mL deionised water (dH_2O) at 4 °C in the dark for 2–4 days. Seeds were then sown in 70 mL pots containing a mix of horticultural sand and peat-based compost (either Levington M3 or Levington F2 + S) in a 2:1 ratio. Plants were grown under short day conditions (8.5:15.5 h day:night at 21 °C at 45–70% RH; Valoya NS1 LED bulbs providing ~150 µmol photons m^{-2} s^{-1}). To initiate flowering and the passage of generations, plants were grown in long-day conditions (16:8 h day:night at 21–23 °C; 45–70% RH; Sylvania GroLux T8 36 W bulbs providing ~ 150 µmol photons m^{-2} s^{-1}). Pots were watered from the bottom 2–3 times a week with reverse osmosis water and trays were frequently rotated within the chamber to minimise positional effects.

For hydroponic experiments (Fig. 1c, d), seeds were vapour-phased sterilised[58] before sowing into 12-well plates. For each well, ~5 seeds were sown in 2 mL of ½ strength Murashige and Skoog (MS) basal salt mixture without vitamins (MS; Sigma-Aldrich M5524) supplemented with 0.5% sucrose, adjusted to pH 5.7. Plates were sealed with micropore tape and stratified at 4 °C in the dark for 2–4 days, after which the plates were moved to long-day conditions for germination and growth. MS media was replaced after 7 days of growth.

Generation of *XVE:ROS1-YFP* plasmids and transgenic lines is described in detail in the supplementary methods of Wilkinson et al.[7]. Five independent *XVE:ROS1-YFP* T3 lines were used in this study: L5, L6, L7, L30, and L32. The *clsy3-1* (SALK_040366), *cmt3-11* (SALK_148381), *nrpe1-11* (SALK_029919) mutants used in this study have been characterised previously[5,18,19,24,53–55]. Homozygous genetic crosses between *clsy3-1*, *cmt3-11* or *nrpe1-11* and L5 were confirmed using primers listed in Supplementary Table 1.

Pathogen cultivation, inoculation, and quantification

All plant inoculations with *Pst-Lux* and *Hpa* were performed within the first 4 h of the light period to minimise the influence of diurnal variation on plant innate immunity[59].

Pseudomonas syringae pv. *tomato* DC3000 *luxCDABE*[29,30] (*Pst-Lux*) was stored in 15–25% (v/v) glycerol stocks at −70 °C. Overnight cultures (16–20 h; 28 °C; shaking at 200 rpm) were grown in King's B (KB) solution supplemented with rifampicin (50 µg/mL) and kanamycin (50 µg/mL). Prior to infection, plants were covered with transparent lids to increase relative humidity and promote stomatal opening. *Pst-Lux* cells were isolated by centrifugation (4000 × *g*; 3 min), washed (10 mM $MgSO_4$), and re-centrifuged (4000 × *g*; 3 min) before resuspending in 10 mM $MgSO_4$. For inoculation, the cell suspension was adjusted to an optical density at 600 nm (OD_{600}) of 0.2 before adding 0.015% v/v silwet L-77 (silwet; LEHLE SEEDS, VIS-30)[30]. For each tray, containing 16–18 pots of plants, 35 mL of inoculum was sprayed onto the surface of leaves, resulting in run-off. Inoculated plants were covered with transparent lids and sealed with parafilm. *Pst-Lux* colonisation was quantified by bioluminescence intensity between 1 and 4 days post infection, using a G:BOX Chemi XRQ gel doc system and ImageJ[30]. Briefly, plants were quenched in darkness for 8 min before taking a long-exposure image (4 min) in the dark. Bright field images (25 ms exposure, with white light) were used to measure plant area and define plant regions. The mean pixel brightness intensity ('mean-grey' value in ImageJ) plus 3x the standard deviation was used to subtract background noise from the bioluminescent images (process > math > subtract). Subsequently, the remaining pixels were used to calculate mean-grey values for each plant-derived region. Thus, the final measurement gives a metric of *Pst-Lux* bioluminescence intensity above background levels, normalised to plant area[30]. Further details can be found in Supplementary Methods.

Hyaloperonospora arabidopsidis isolate Waco9 (*Hpa*) was maintained on hypersusceptible *NahG*-expressing Arabidopsis plants of the ecotype *Wassilewskija* (Ws). For inoculations, infected leaves from host plants were washed with dH_2O, filtered through Miracloth, and quantified using a hemacytometer (Improved Neubauer, Hawksley, UK; Depth 0.1 mm, 1/400 mm^2). Spore density was adjusted to 1×10^5 spores/mL and inoculum sprayed onto the surface of leaves until

droplets covered all leaves. Five days after infection, aerial tissue was collected in 100% ethanol. Plant material was then stained with trypan blue, as described by Stassen et al.[46]. Individual leaves were microscopically analysed (Optika Italy Lab-20 binocular stereozoom microscope), based on previously reported hallmarks of *Hpa* colonisation and pathogenesis[31]. Briefly, leaves were assigned to four *Hpa* colonisation classes: I: no hyphal colonisation; II: limited hyphal colonisation with 8 or less conidiophores; III: extensive hyphal colonisation with more than 8 conidiophores; and class IV: extensive hyphal colonisation with conidiophores and oospore(s).

Chemical treatments

Chemical treatments were performed within the first 4 h of the light period. 17β-estradiol (E2; Sigma-Aldrich E8875) was dissolved in dimethyl sulfoxide (DMSO; Sigma-Aldrich D4540) to a final stock concentration of 50 mM and stored at −20 °C. At the time of treatment, stock aliquots were diluted in dH_2O to the desired working solution. Mock solutions (DMSO treatments) consisted of dH_2O plus an equivalent volume of DMSO. In soil-based experiments, E2/DMSO solutions were supplemented with 0.015% (v/v) silwet and sprayed onto the surface of leaves (20 mL per tray; 1.1 – 1.5 mL per pot). Unless stated otherwise, E2- and DMSO-treatment refers to a dual spray treatment of soil-grown plants at 14 and 18 days after sowing (DAS) with 10 µM and 25 µM E2 or 0.02% and 0.05% DMSO (Fig. 2a). For hydroponic experiments (Fig. 1c, d), E2/DMSO was added directly to the wells using stock solutions with no added silwet.

Stock solutions of 5-Azacytidine (5-Aza; Sigma #A2385) were prepared in dH_2O at a concentration of 24.6 mM (6 mg/mL). Working solutions were prepared in ddH_2O to a final concentration of 100 µM and supplemented with 0.015% (v/v) silwet. Mock treatments consisted of dH_2O and silwet only. To minimise health risks of spraying 5-Aza solution, a single droplet containing either 5-Aza or mock solution was carefully applied to the apical meristem of every seedling. Droplet volumes were: 6 µL at 7 days after sowing (DAS); 8 µL at 9 and 11 DAS; and 10 µL at 13 and 16 DAS.

Epifluorescence microscopy

Epi-fluorescence microscopy to quantify accumulation of ROS1-YFP in living plants was performed using a Leica M165 FC fluorescent stereo microscope (Objective: 1x/0.06; ET-GFP filter set: 470/40 nm excitation, 495 nm dichroic and 525/50 nm emission) with a CoolLED pE-300 illumination system, controlled by Leica LAS X software v3.7.4.23463. ROS1-YFP intensity was quantified in ImageJ, using the background-subtracted mean-grey value, normalised by plant area. To account for autofluorescence, ROS1-YFP signal was calculated as a relative fold change compared to DMSO-treated plants.

To validate nuclear localisation of ROS1-YFP signal, leaves were detached from soil-grown plants 24 h after spraying with 25 µM E2 and vacuum infiltrated with DAPI solution (2 µg/mL) for 2–3 min. Leaves were mounted on slides and imaged using a Leica DM6B epi-fluorescence microscope (light source: CoolLED pE-2; Objective: HC PL Fluotar 40x/0.80; ET-DAPI filter set: 350/50 nm excitation, 400 nm dichroic, and 460/50 nm emission; ET-GFP filter set: 470/40 nm excitation, 495 nm dichroic, and 525/50 nm emission) controlled by Leica LAS X v3.7.3.23245 software. Using ImageJ, the brightness and contrast were increased equally for: BF images (20% and 10%, respectively); DAPI images (60% and 70%, respectively); and YFP images (40% and 70%, respectively). DAPI and YFP images were pseudo-coloured cyan and yellow, respectively, using ImageJ.

Reverse transcriptase-quantitative PCR (RT-qPCR)

For each biological replicate in each experiment (Fig. 2e; Supplementary Fig. 12a), aerial tissue of ~10 plants were harvested together, flash frozen in liquid nitrogen, and stored at −70 °C. One hundred milligrams of ground tissue was used for RNA extractions using the RNeasy plant mini kit (Qiagen, #74904) and 800 ng of RNA was used for cDNA synthesis using the 'Maxima First Strand cDNA Synthesis Kit for RT-qPCR, with dsDNase' kit (Thermo Scientific, K1672). Diluted cDNA (1:5) was used for RT-qPCR using SsoAdvanced SYBR Green Supermix (BioRad, 1725270), ROS1-specific primers (Supplementary Table 1), and a Rotor-Gene Q (Qiagen) real-time PCR cycler. Take off values and primer efficiencies were calculated using the Rotor-Gene Q Series software (v2.1.0). Relative expression values were calculated as described in Wilkinson et al.[7], using *MON1* (AT2G28390) and *UBC21* (AT5G25760) as stably-expressed reference genes[60] and a DMSO-treated sample as the calibrator.

Next-generation sequencing: material harvest, extractions, and sequencing

For short-read sequencing experiments (Figs. 3, 5), 48 h after treating Col-0, L5 and/or L7 twice with E2 or DMSO (Fig. 2a), aerial tissues were collected from ~6 pots in a single tray to form a single biological replicate ($n = 3$). Material was snap frozen in liquid nitrogen and ground to a fine powder using liquid nitrogen and a mortar and pestle. Several ~100 mg aliquots of tissue were stored at −70 °C for each biological replicate. Individual aliquots, derived from the same pool of ground tissue, were used for genomic DNA and total RNA extractions, using the DNeasy Plant Mini Kit (Qiagen 69104), and TRIzol Reagent (Thermo Fisher Scientific 15596026), respectively. Genomic DNA was used for whole-genome bisulfite sequencing (WGBS); RNA was used for polyA-enriched RNA-sequencing (mRNA-seq), ribosome-depleted RNA-sequencing (RNA-seq), and/or small RNA sequencing (sRNA-seq; 18–30 nt). Library preparation and sequencing were performed by BGI Genomics using the DNA nanoball (DNB) sequencing (DNBSEQ™) G400 platform.

For long-read DNA methylation sequencing data of E2- and DMSO-treated *XVE:ROS1-YFP* L5 (as depicted in Fig. 2a), we employed Oxford Nanopore Sequencing Technology (ONT-seq), as described by Wilkinson et al. (2023). Briefly, for each biological replicate ($n = 3$) per treatment and at 20 DAS (2 days after the final E2 treatment), ~100 plants derived from 1 tray (~ 500 mg fresh weight) were snap frozen in liquid nitrogen and ground to a fine powder using a pestle and mortar. DNA was extracted using the NucleoBond® HMW DNA kit (Macherey Nagel, 740160.20) and library preparation was done using the ONT Rapid Barcoding kit (ONT, SQK-RBK004). Sequencing was performed on FLO-MIN106 flow cells, in combination with the Flow Cell Wash Kit (ONT, EXP-WSH004). Summary statistics for all sequencing data are provided in Supplementary Data 7.

Next-generation sequencing analysis: alignment and quantification

Reads from WGBS, RNA-seq, mRNA-seq, and sRNA-seq were analysed for adaptors and read quality using FastQC v0.12.1 and MultiQC v1.21[61]. For WGBS data, reads were aligned to the TAIR10 genome and called for cytosine methylation using Bismark v0.24.1[62]. DMCs and DMRs were called using the R package DSS v2.46.0[50,51]. Transcriptomic sequencing (RNA- and mRNA-seq) data were aligned and read counts per feature were quantified using STAR v2.7.9a[63], the TAIR10 genome, and a custom annotation file that merged the Araport11 annotation[64] and a gene-like annotation file of TEs[65]. Library normalisation and DEG calling were performed using the R package DEseq2 v1.42.1[66]. Due to a confounding effect related to the default normalisation technique, the counts were normalised using a suite of extremely stably expressed genes in Arabidopsis[60,67], as recommended by the DESeq2 user guide (v1.42.0) and Love et al. (2014) (Supplementary Methods). sRNA reads with perfect matches to known ribosomal RNA sequences were removed using Bowtie v1.3.1[68] and the RNAcentral database of non-coding RNA sequences (accessed: 23/01/2024)[69]. Filtered reads were then mapped to the TAIR10 genome and de novo clusters defined

using ShortStack v.4.0.3[35,36]. Differentially expressed clusters were called using the R package DEseq2 v1.42.1.

ONT-seq reads were base called and filtered using Guppy v6.5.7 and the 'dna_r9.4.1_450bps_hac.cfg' model. Methylated cytosines were identified using the 'model.dp2.CNN.arabnrice2-1_120m_R9.4plus_tem.bn13_sn16.both_bilstm.epoch6.ckpt' model from DeepSignal-plant v0.1.4[49] in conjunction with Tombo v1.5.1 and the reference genome Col-CEN v1.2[47]. DMCs were called using the R package DSS v2.46.0. Further information on the parameters used are provided in the Supplementary Methods. Summary statistics are provided in Supplementary Data 7.

Next-generation sequencing analysis: annotation

For all short-read sequencing data (WGBS, RNA-seq, mRNA-seq, sRNA-seq), features were annotated using a custom annotation file that merged the Araport11 annotation[64] and a gene-like annotation file of TEs[65] in the TAIR10 assembly (Supplementary Methods). For DMRs and DECs, overlaps with features were identified using the R packages Genomation v1.34.0[70] and GenomicRanges v1.54.1[71]. Promoters were defined as −1kb from the TSS, or to the next nearest gene, whichever was shorter. Downstream regions were defined as +1 kb from the transcriptional termination site. In cases where a DMR or DEC overlapped more than one feature, a single annotation was chosen based on a hierarchy (Supplementary Methods). For each nuclear chromosome in the TAIR10 assembly, the start of the pericentromere was defined as the midpoint of the first 100 kb bin in a string of at least 5 neighbouring 100 kb bins for which TE density > gene density. The end of the pericentromere was defined as the midpoint of the last bin in a string of at least 5 neighbouring bins where TE density > protein-coding gene density (Chr1: 12450000-17650000, Chr2:1250000-7050000, Chr3: 10450000-16250000, Chr4: 1650000-6350000, Chr5: 9750000-14650000). Genome bins were created using bedtools v2.31.0[72].

For long-read ONT-seq data, the Araport11-based annotation file for the Col-CEN assembly was used in combination with the intact complete EDTA repeat annotation file (https://github.com/schatzlab/Col-CEN/tree/main/v1.2; accessed 21/09/2023)[47]. Pericentromeres were defined as done for the TAIR10 assembly (Chr1: 12050000-19850000, Chr2: 1350000-9850000, Chr3: 10350000-18950000, Chr4: 1750000-9850000, Chr5: 9650000-18150000), but centromere coordinates were used as defined by Naish et al. (2021) (Chr1: 14840000-17560000, Chr2: 3823000-6046000, Chr3: 13597000-15734000, Chr4: 4204000-6978000, Chr5: 11784000-14560000).

Next-generation sequencing analysis: gene ontology enrichment

Enrichment of biological process gene ontology (GO) terms was performed using R packages clusterProfiler v4.14.6[73] (function: 'enrichGO'; options: 'pvalueCutoff = 0.05', 'qvalueCutoff = 0.05', 'OrgDb = "org.At.tair.db"', 'keyType = "TAIR"', 'ont = "BP"', 'minGSSize = 10', 'maxGSSize = 500', 'universe = all_proteinGenes_≥10counts_≥6samples') and org.At.tair.db v3.20.0. GO terms were classed as enriched if they had p_{adj}-values < 0.05 (Benjamini and Hochberg correction). GO semantic similarity analysis was performed using the R package GOSemSim v2.28.1[74] (function: 'godata'; options: 'OrgDb = "org.At.tair.db"', 'ont = "BP"'). The object resulting from this analysis was used in conjunction with clusterProfiler to create a simplified enriched GO list (function: 'simplify'; options: 'cutoff=0.7', 'semData=SemSimAnalysis_object', 'by = "p.adjust"', 'select_fun=min'). All GO terms, raw and simplified, are provided in Supplementary Data 3.

Next-generation sequencing analysis: genome-wide scan of *cis*-regulated candidate genes

Cis-regulated genes in this study refer to protein-coding genes whose expression is negatively regulated by DNA methylation in the promoter region, as previously described for other ROS1 targets[24,25]. Given that ROS1 targets are often antagonistically regulated by Pol-IV-dependent RdDM, which requires 24 nt sRNAs and existing methylated cytosines (Supplementary Fig. 9a)[16,17,20,22,24,26], *cis*-regulated candidates were defined as protein-coding genes that were significantly upregulated in E2-treated plants, and contained a hypomethylated DMR, and/or a downregulated 24 nt DEC in their promoter region in both independent *XVE:ROS1-YFP* lines.

Expression of *cis*-regulated candidates in *mddcc* and Col-0 plants (Supplementary Fig. 9b) were analysed using FPKM values provided by He et al.[39]. Of our 173 *cis*-regulated candidates, five hypothetical-protein genes did not have reported FPKM values in this study (*AT1G28005, AT2G14825, AT3G29645, AT4G07995, AT5G23115*).

Statistical analyses and generation of plots

All specific statistical tests have been explicitly mentioned in the main text or figure legends. Significant effects identified by one- or two-way ANOVAs were followed by a Tukey's post-hoc test; where assumptions of normality and/or homoscedasticity were not met, a Kruskal-Wallis test followed by Conover-Iman[75] post-hoc comparisons was used. Unless otherwise specified, plots were generated using the R package ggplot2 v3.5.0 and statistical analyses were performed using base R v4.3.2 or the R package rstatix v0.7.2. Plots of DECs along chromosomes were generated using the R package 'KaryoploteR' v1.28.0[76].

Reporting summary

Further information on research design is available in the Nature Portfolio Reporting Summary linked to this article.

Data availability

The ChIP-seq data for Myc-ROS1 and ROS1-FLAG were analysed using data uploaded to the NCBI Gene Expression Omnibus (GEO) under accession codes GSE245961 and GSE282076, respectively. Raw data for one biological replicate per treatment has already been published for the ONT-seq[7] and uploaded to GEO under accession code GSE211295. The additional ONT-seq samples are newly available on GEO under the accession code GSE304524. WGBS data of *nrpe1-11* and *cmt3-11* mutants were reanalysed from Wilkinson et al.[7] and Briffa et al.[77] under accession codes GSE199625 and GSE204837, respectively. WGBS data of 5-Aza-treated Arabidopsis are from Griffin et al.[57] and are available under the GEO accession code GSE80300. RNA-seq of *35S:TET1* lines is from Ji et al.[33] and are available under the GEO accession code GSE93024. All newly generated data from RNA-seq, sRNA-seq, and WGBS are available under GEO accession codes GSE304523, GSE304519, and GSE304520, respectively. All other experimental data generated in this study are provided as Supplementary Data files and/or in the Source Data file. Source data are provided with this paper.

References

1. De Kesel, J. et al. The induced resistance lexicon: do's and don'ts. *Trends Plant Sci.* **26**, 685–691 (2021).
2. Cooper, A. & Ton, J. Immune priming in plants: from the onset to transgenerational maintenance. *Essays Biochem.* **66**, 635–646 (2022).
3. Bozarth, R. F. & Ross, A. F. Systemic resistance induced by localized virus infections: extent of changes in uninfected plant parts. *Virology* **24**, 446–455 (1964).
4. Luna, E., López, A., Kooiman, J. & Ton, J. Role of NPR1 and KYP in long-lasting induced resistance by β-aminobutyric acid. *Front. Plant Sci.* **5**, 184 (2014).
5. López Sánchez, A., Stassen, J. H. M., Furci, L., Smith, L. M. & Ton, J. The role of DNA (de)methylation in immune responsiveness of Arabidopsis. *Plant J.* **88**, 361–374 (2016).

6. Wilkinson, S. W. et al. Surviving in a Hostile World: Plant Strategies to Resist Pests and Diseases. *Annu. Rev. Phytopathol.* **57**, 505–529 (2019).
7. Wilkinson, S. W. et al. Long-lasting memory of jasmonic acid-dependent immunity requires DNA demethylation and ARGONAUTE1. *Nat. Plants* **9**, 81–95 (2023).
8. Furci, L. et al. Heritable induced resistance in Arabidopsis thaliana: tips and tools to improve effect size and reproducibility. *Plant Direct* **7**, e523 (2023).
9. Hannan Parker, A., Wilkinson, S. W. & Ton, J. Epigenetics: a catalyst of plant immunity against pathogens. *N. Phytol.* **233**, 66–83 (2022).
10. Johannes, F. et al. Assessing the impact of transgenerational epigenetic variation on complex traits. *PLOS Genet.* **5**, e1000530 (2009).
11. Hofmeister, B. T., Lee, K., Rohr, N. A., Hall, D. W. & Schmitz, R. J. Stable inheritance of DNA methylation allows creation of epigenotype maps and the study of epiallele inheritance patterns in the absence of genetic variation. *Genome Biol.* **18**, 155 (2017).
12. Long, J. et al. Nurse cell–derived small RNAs define paternal epigenetic inheritance in Arabidopsis. *Science* **373**, eabh0556 (2021).
13. Martinho, C. et al. CHROMOMETHYLTRANSFERASE3/KRYPTONITE maintains the sulfurea paramutation in Solanum lycopersicum. *Proc. Natl. Acad. Sci. USA* **119**, e2112240119 (2022).
14. van Hulten, M., Pelser, M., van Loon, L. C., Pieterse, C. M. J. & Ton, J. Costs and benefits of priming for defense in Arabidopsis. *Proc. Natl. Acad. Sci. USA* **103**, 5602–5607 (2006).
15. López Sánchez, A., Pascual-Pardo, D., Furci, L., Roberts, M. R. & Ton, J. Costs and benefits of transgenerational induced resistance in Arabidopsis. *Front. Plant Sci.* **12**, 644999 (2021).
16. Zhang, H., Lang, Z. & Zhu, J.-K. Dynamics and function of DNA methylation in plants. *Nat. Rev. Mol. Cell Biol.* **19**, 489–506 (2018).
17. Cuerda-Gil, D. & Slotkin, R. K. Non-canonical RNA-directed DNA methylation. *Nat. Plants* **2**, 1–8 (2016).
18. Zhou, M. et al. The CLASSY family controls tissue-specific DNA methylation patterns in Arabidopsis. *Nat. Commun.* **13**, 244 (2022).
19. Zhou, M., Palanca, A. M. S. & Law, J. A. Locus-specific control of the de novo DNA methylation pathway in Arabidopsis by the CLASSY family. *Nat. Genet.* **50**, 865–873 (2018).
20. Sigman, M. J. et al. An siRNA-guided ARGONAUTE protein directs RNA polymerase V to initiate DNA methylation. *Nat. Plants* **7**, 1461–1474 (2021).
21. Gouil, Q. & Baulcombe, D. C. DNA Methylation Signatures of the Plant Chromomethyltransferases. *PLOS Genet.* **12**, e1006526 (2016).
22. Harris, C. J., Zhong, Z., Ichino, L., Feng, S. & Jacobsen, S. E. H1 restricts euchromatin-associated methylation pathways from heterochromatic encroachment. *eLife* **12**, RP89353 (2024).
23. Zhang, H., Gong, Z. & Zhu, J.-K. Active DNA demethylation in plants: 20 years of discovery and beyond. *J. Integr. Plant Biol.* **64**, 2217–2239 (2022).
24. Tang, K., Lang, Z., Zhang, H. & Zhu, J.-K. The DNA demethylase ROS1 targets genomic regions with distinct chromatin modifications. *Nat. Plants* **2**, 1–10 (2016).
25. Halter, T. et al. The Arabidopsis active demethylase ROS1 cis-regulates defence genes by erasing DNA methylation at promoter-regulatory regions. *eLife* **10**, e62994 (2021).
26. Deng, L. et al. Occupancy-based mechanism is the chief mode of ROS1 function in preventing DNA hypermethylation. *Nat. Plants* **12**, 863–879 (2026).
27. Zuo, J., Niu, Q.-W. & Chua, N.-H. An estrogen receptor-based transactivator XVE mediates highly inducible gene expression in transgenic plants. *Plant J.* **24**, 265–273 (2000).
28. Siligato, R. et al. MultiSite gateway-compatible cell type-specific gene-inducible system for plants. *Plant Physiol.* **170**, 627–641 (2016).
29. Fan, J., Crooks, C. & Lamb, C. High-throughput quantitative luminescence assay of the growth in planta of Pseudomonas syringae chromosomally tagged with Photorhabdus luminescens luxCDABE. *Plant J.* **53**, 393–399 (2008).
30. Furci, L., Pascual-Pardo, D. & Ton, J. A rapid and non-destructive method for spatial–temporal quantification of colonization by Pseudomonas syringae pv. tomato DC3000 in Arabidopsis and tomato. *Plant Methods* **17**, 126 (2021).
31. Schwarzenbacher, R. E. et al. The IBI1 receptor of β-aminobutyric acid interacts with VOZ transcription factors to regulate abscisic acid signaling and callose-associated defense. *Mol. Plant* **13**, 1455–1469 (2020).
32. Wang, M. et al. Histone H3 lysine 4 methylation recruits DNA demethylases to enforce gene expression in Arabidopsis. *Nat. Plants* **11**, 206–217 (2025).
33. Ji, L. et al. TET-mediated epimutagenesis of the Arabidopsis thaliana methylome. *Nat. Commun.* **9**, 895 (2018).
34. Zhang, X., Zhang, Y., Wang, C. & Wang, X. T. E. T. (Ten-eleven translocation) family proteins: structure, biological functions and applications. *Sig Transduct. Target Ther.* **8**, 1–20 (2023).
35. Axtell, M. J. ShortStack: Comprehensive annotation and quantification of small RNA genes. *RNA* **19**, 740–751 (2013).
36. Shahid, S. & Axtell, M. J. Identification and annotation of small RNA genes using ShortStack. *Methods* **67**, 20–27 (2014).
37. Charvin, M. et al. Single-cytosine methylation at W-boxes repels binding of WRKY transcription factors through steric hindrance. *Plant Physiol.* **192**, 77–84 (2023).
38. Yu, A. et al. Dynamics and biological relevance of DNA demethylation in Arabidopsis antibacterial defense. *PNAS* **110**, 2389–2394 (2013).
39. He, L. et al. DNA methylation-free Arabidopsis reveals crucial roles of DNA methylation in regulating gene expression and development. *Nat. Commun.* **13**, 1335 (2022).
40. Zavaliev, R. & Dong, X. NPR1, a key immune regulator for plant survival under biotic and abiotic stresses. *Mol. Cell* **84**, 131–141 (2024).
41. Tada, Y. et al. Plant immunity requires conformational changes [corrected] of NPR1 via S-nitrosylation and thioredoxins. *Science* **321**, 952–956 (2008).
42. Kneeshaw, S., Gelineau, S., Tada, Y., Loake, G. J. & Spoel, S. H. Selective protein denitrosylation activity of thioredoxin-*h*5 modulates plant immunity. *Mol. Cell* **56**, 153–162 (2014).
43. Herbst, J., Li, Q.-Q. & De Veylder, L. Mechanistic insights into DNA damage recognition and checkpoint control in plants. *Nat. Plants* **10**, 539–550 (2024).
44. Furci, L. et al. Identification and characterisation of hypomethylated DNA loci controlling quantitative resistance in Arabidopsis. *eLife* **8**, e40655 (2019).
45. Meng, D. et al. Limited contribution of DNA methylation variation to expression regulation in Arabidopsis thaliana. *PLoS Genet.* **12**, e1006141 (2016).
46. Stassen, J. H. M. et al. The relationship between transgenerational acquired resistance and global DNA methylation in Arabidopsis. *Sci. Rep.* **8**, 14761 (2018).
47. Naish, M. et al. The genetic and epigenetic landscape of the Arabidopsis centromeres. *Science* **374**, eabi7489 (2021).
48. Naish, M. & Henderson, I. R. The structure, function, and evolution of plant centromeres. *Genome Res.* **34**, 161–178 (2024).
49. Ni, P. et al. Genome-wide detection of cytosine methylations in plant from Nanopore data using deep learning. *Nat. Commun.* **12**, 5976 (2021).
50. Feng, H., Conneely, K. N. & Wu, H. A Bayesian hierarchical model to detect differentially methylated loci from single nucleotide resolution sequencing data. *Nucleic Acids Res.* **42**, e69 (2014).

51. Park, Y. & Wu, H. Differential methylation analysis for BS-seq data under general experimental design. *Bioinformatics* **32**, 1446–1453 (2016).
52. Felgines, L. et al. CLSY docking to Pol IV requires a conserved domain critical for small RNA biogenesis and transposon silencing. *Nat. Commun.* **15**, 10298 (2024).
53. Chan, S. W.-L. et al. RNAi, DRD1, and histone methylation actively target developmentally important non-CG DNA methylation in arabidopsis. *PLOS Genet.* **2**, e83 (2006).
54. Stroud, H., Greenberg, M. V. C., Feng, S., Bernatavichute, Y. V. & Jacobsen, S. E. Comprehensive analysis of silencing mutants reveals complex regulation of the arabidopsis methylome. *Cell* **152**, 352–364 (2013).
55. Pontier, D. et al. Reinforcement of silencing at transposons and highly repeated sequences requires the concerted action of two distinct RNA polymerases IV in Arabidopsis. *Genes Dev.* **19**, 2030–2040 (2005).
56. Dowen, R. H. et al. Widespread dynamic DNA methylation in response to biotic stress. *PNAS* **109**, E2183–E2191 (2012).
57. Griffin, P. T., Niederhuth, C. E. & Schmitz, R. J. A comparative analysis of 5-azacytidine- and zebularine-induced DNA demethylation. *G3 (Bethesda)* **6**, 2773–2780 (2016).
58. Lindsey, B. E., Rivero, L., Calhoun, C. S., Grotewold, E. & Brkljacic, J. Standardized method for high-throughput sterilization of Arabidopsis seeds. *J. Vis. Exp.* 56587 (2017).
59. Lu, H., McClung, C. R. & Zhang, C. Tick Tock: Circadian regulation of plant innate immunity. *Annu. Rev. Phytopathol.* **55**, 287–311 (2017).
60. Czechowski, T., Stitt, M., Altmann, T., Udvardi, M. K. & Scheible, W.-R. Genome-wide identification and testing of superior reference genes for transcript normalization in arabidopsis. *Plant Physiol.* **139**, 5–17 (2005).
61. Ewels, P., Magnusson, M., Lundin, S. & Käller, M. MultiQC: summarize analysis results for multiple tools and samples in a single report. *Bioinformatics* **32**, 3047–3048 (2016).
62. Krueger, F. & Andrews, S. R. Bismark: a flexible aligner and methylation caller for Bisulfite-Seq applications. *Bioinformatics* **27**, 1571–1572 (2011).
63. Dobin, A. et al. STAR: ultrafast universal RNA-seq aligner. *Bioinformatics* **29**, 15–21 (2013).
64. Cheng, C.-Y. et al. Araport11: a complete reannotation of the Arabidopsis thaliana reference genome. *Plant J.* **89**, 789–804 (2017).
65. Panda, K. & Slotkin, R. K. Long-read cDNA sequencing enables a "gene-like" transcript annotation of transposable elements. *Plant Cell* **32**, 2687–2698 (2020).
66. Love, M. I., Huber, W. & Anders, S. Moderated estimation of fold change and dispersion for RNA-seq data with DESeq2. *Genome Biol.* **15**, 550 (2014).
67. Hong, S. M., Bahn, S. C., Lyu, A., Jung, H. S. & Ahn, J. H. Identification and testing of superior reference genes for a starting pool of transcript normalization in arabidopsis. *Plant Cell Physiol.* **51**, 1694–1706 (2010).
68. Langmead, B., Trapnell, C., Pop, M. & Salzberg, S. L. Ultrafast and memory-efficient alignment of short DNA sequences to the human genome. *Genome Biol.* **10**, R25 (2009).
69. RNAcentral Consortium RNAcentral 2021: secondary structure integration, improved sequence search and new member databases. *Nucleic Acids Res.* **49**, D212–D220 (2021).
70. Akalin, A., Franke, V., Vlahoviček, K., Mason, C. E. & Schübeler, D. Genomation: a toolkit to summarize, annotate and visualize genomic intervals. *Bioinformatics* **31**, 1127–1129 (2015).
71. Lawrence, M. et al. Software for computing and annotating genomic ranges. *PLOS Comput. Biol.* **9**, e1003118 (2013).
72. Quinlan, A. R. & Hall, I. M. BEDTools: a flexible suite of utilities for comparing genomic features. *Bioinformatics* **26**, 841–842 (2010).
73. Wu, T. et al. clusterProfiler 4.0: a universal enrichment tool for interpreting omics data. *Innovation* **2**, 100141 (2021).
74. Yu, G. Gene Ontology semantic similarity analysis using GOSemSim. *Methods Mol. Biol.* **2117**, 207–215 (2020).
75. Conover, W. J. & Iman, R. L. *Multiple-Comparisons Procedures. Informal Report*. https://www.osti.gov/biblio/6057803 https://doi.org/10.2172/6057803 (1979).
76. Gel, B. & Serra, E. karyoploteR: an R/Bioconductor package to plot customizable genomes displaying arbitrary data. *Bioinformatics* **33**, 3088–3090 (2017).
77. Briffa, A. et al. Millennia-long epigenetic fluctuations generate intragenic DNA methylation variance in *Arabidopsis* populations. *Cell Syst.* **14**, 953–967.e17 (2023).

Acknowledgements

We thank H. Hipperson for conducting the ONT-seq, D. Pascual-Pardo for horticultural support, S. Shahid for advice on sRNA-seq analyses, and D. Baulcombe for advice on cytosine sub-context methylation analyses.

Author contributions

A.H.P. and J.T. conceptualised the study, with supervision from S.A.R., L.M.S., S.W.W., and J.T. Funding was acquired by J.T., L.M.S., and S.A.R. A.H.P. conducted the experiments and collected data, with assistance from P.Z., K.Y.M., and L.T. Data analysis and visualisation were performed by A.H.P. with guidance from S.W.W., S.A.R., L.M.S., and J.T. A.H.P. and J.T. wrote the original manuscript, with input from all authors.

Funding

This work was supported by a European Research Council (ERC) Advanced Grant to JT and SAR ("PlantMemo"; 101199639) and two grants from UK Research and Innovation (UKRI): a Biotechnology and Biological Sciences Research Council (BBSRC) White Rose DTP Studentship (BB/T007222/1: project 2449363), and a BBSRC Industrial Partnership Award to JT, SAR, and LMS (BB/W015250/1).

Competing interests

The authors declare no competing interests.

Additional information

Supplementary information The online version contains supplementary material available at https://doi.org/10.1038/s41467-026-78905-y.

Correspondence and requests for materials should be addressed to Adam Hannan Parker or Jurriaan Ton.

Peer review information *Nature Communications* thanks the anonymous reviewers for their contribution to the peer review of this work. A peer review is available.

Reprints and permissions information is available at http://www.nature.com/reprints

Publisher's note Springer Nature remains neutral with regard to jurisdictional claims in published maps and institutional affiliations.

Open Access This article is licensed under a Creative Commons Attribution 4.0 International License, which permits use, sharing, adaptation, distribution and reproduction in any medium or format, as long as you give appropriate credit to the original author(s) and the source, provide a link to the Creative Commons licence, and indicate if changes were made. The images or other third party material in this article are included in the article's Creative Commons licence, unless indicated otherwise in a credit line to the material. If material is not included in the article's Creative Commons licence and your intended use is not permitted by statutory regulation or exceeds the permitted use, you will need to obtain permission directly from the copyright holder. To view a copy of this licence, visit http://creativecommons.org/licenses/by/4.0/.

© The Author(s) 2026

This Article in Press is shared early to give you faster access to new research. It is citable and carries a permanent DOI. The final edited version will replace it automatically.